


# Disentangling superconductor and dielectric microwave losses in submicrometer Nb/SiO<sub>2</sub> interconnects using a multimode microstrip resonator

Cougar A. T. Garcia<sup>1,2,\*</sup>, Nancyjane Bailey,<sup>1</sup> Chris Kirby,<sup>1</sup> Joshua A. Strong<sup>1</sup>,  
Vladimir V. Talanov,<sup>1</sup> Anna Yu. Herr<sup>1,†</sup> and Steven M. Anlage<sup>2,3</sup>

<sup>1</sup>Northrop Grumman Corporation, Baltimore, Maryland 21240, USA

<sup>2</sup>Department of Materials Science and Engineering, University of Maryland, College Park, Maryland 20742, USA

<sup>3</sup>Quantum Materials Center, Physics Department, University of Maryland, College Park, Maryland 20742, USA

 (Received 26 May 2023; revised 17 November 2023; accepted 20 November 2023; published 28 February 2024)

An understanding of the origins of power loss in superconducting interconnects is essential for the energy efficiency and scalability of superconducting digital logic. At microwave frequencies, power dissipates in both the superconducting wires and the dielectric and these losses can be of comparable magnitude. We describe an approach to accurately disentangle such losses by exploiting their frequency dependence in a multimode transmission-line resonator. This is supported by the concept of a resonator geometric factor extracted from the Ansys High Frequency Structure Simulator (HFSS), a commercial three-dimensional finite-element method (FEM) that we adopt for solving a superconductor interior. Using the technique, we have optimized a planarized fabrication process of reciprocal quantum logic (RQL) for the minimum interconnect loss at 4.2 K and gigahertz frequencies. The microstrip interconnects are composed of niobium (Nb) insulated by silicon dioxide (SiO<sub>2</sub>) made from a tetraethoxysilane (TEOS) precursor. Two process generations use damascene fabrication and the third one uses Cloisonné fabrication. For all three, SiO<sub>2</sub> exhibits a dielectric loss tangent  $\tan \delta = 0.0012 \pm 0.0001$ , independent of the Nb wire width over 0.25–4  $\mu\text{m}$ . The intrinsic microwave resistance  $R_s$  of Nb varies with both the process and the wire width. For damascene fabrication, scanning transmission electron microscopy (STEM) and energy-dispersive x-ray spectroscopy (EDS) reveal that plasma oxidation and grain-growth orientation increase  $R_s$  above the Bardeen-Cooper-Schrieffer (BCS) resistance  $R_{\text{BCS}} \approx 17 \mu\Omega$  at 10 GHz. For Cloisonné fabrication, we demonstrate  $R_s = 13 \pm 1.4 \mu\Omega$  down to 0.25  $\mu\text{m}$  wire width, which is below  $R_{\text{BCS}}$  and arguably the lowest microwave resistance reported for Nb at 4.2 K.

DOI: [10.1103/PhysRevApplied.21.024056](https://doi.org/10.1103/PhysRevApplied.21.024056)

## I. INTRODUCTION

Single-flux-quantum (SFQ) digital superconductor electronics (SCE) employs Josephson junctions to form the logic gates and superconducting interconnects to deliver clock and power to various circuits on the chip and to propagate bits of information between them [1–3]. Unlike the voltage-biased complementary metal-oxide-semiconductor (CMOS) transistor switching between open- and short-circuit states, the current-biased Josephson junction has zero resistance except during switching events. The junction switch produces a picosecond pulse of a millivolt amplitude that carries a magnetic flux quantum  $\Phi_0 \approx 2.067 \times 10^{-15} \text{ Wb}$  [4]. The presence or absence of the pulse corresponds to a digital “1” or “0.” Exploiting

the pulse energy of only  $10^{-19} \text{ J}$  and the available clock rate up to 120 GHz [5], to compete with CMOS computing technologies, the SFQ-logic community is focusing on the energy efficiency and scalability [6,7].

Energy-efficient SFQ-logic families, including the quantum flux parametron (QFP) [8], reciprocal quantum logic (RQL) [9], energy-efficient single flux quantum (eSFQ) logic [10] and the adiabatic quantum flux parametron (AQFP) [11], minimize or eliminate a static power dissipation hampering the original rapid single-flux-quantum (RSFQ) logic [1,2]. Nevertheless, analogous to Cu–low- $k$  interconnects dominating a CMOS logic power budget [12, 13], superconducting interconnects can notably impact the power dissipation of the energy-efficient SFQ logic. This is associated with data transfer, rf bias, and clock-distribution networks. For instance, RQL has been reported to consume 300 times less power than CMOS logic, including the cooling overhead in large-scale systems [9]. However, a metamaterial zeroth-order resonator (ZOR) for the

\*cougar.garcia@ngc.com

†Present address: IMEC-USA, Kissimmee, Florida 34744, USA

clock and power distribution at gigahertz frequencies dissipates twice the logic power, due to the transmission-line loss [14].

The interconnect density is one of the main factors limiting the scalability of all forms of superconducting logic [15]. The performance capability of a chip increases with the total number of logic gates, calling for more layers of high-speed low-loss interconnects with smaller pitch (the sum of the wire width and spacing) [7,16,17]. Chemical mechanical polishing or planarization (CMP) [18] allows one to fabricate a logic chip with up to ten wiring layers [19], by removing topography left from the previous layer patterning and deposition [20–22]. However, due to the high affinity of Nb for oxygen (O), carbon (C), hydrogen (H), and nitrogen (N) [23], processes including CMP, chemical vapor deposition (CVD) of silicon dioxide (SiO<sub>2</sub>) insulator from a tetraethoxysilane Si(OC<sub>2</sub>H<sub>5</sub>)<sub>4</sub> precursor (TEOS), reactive ion etching (RIE), and oxygen-plasma treatment may contaminate Nb [24] and exacerbate its microwave loss, which has not been investigated. In our work, both damascene (metal CMP) and Cloisonné (dielectric CMP) planarized fabrication will be utilized and compared. An elemental material analysis will reveal sources of extraneous resistive loss in the submicron Nb interconnects.

The microstrip transmission line (MTL) [25] and strip line are the ubiquitous superconducting interconnects, with 700-GHz analog bandwidth. They enable a basic building block for clock- and power-distribution systems [14,26,27], a passive transmission line (PTL) for low-bandwidth data (35–50 GHz) with 7–10 flux quanta per bit [27], a PTL for high-bandwidth data (350 GHz) with a single flux quantum per bit [28,29], and a delay-line memory [30]. Unlike the power dissipation of CMOS interconnects governed by the metal (Al or Cu) loss, the power dissipation of SCE interconnects is governed by both the superconductor and dielectric losses, which can be of comparable magnitude. Affecting the circuit integration, the propagation distance of the SFQ pulse on PTL scales with a transmission-line resonator figure of merit, the quality factor ( $Q$  factor) [29]. Our paper is concerned with simultaneously extracting the superconductor microwave resistance  $R_s$  and the dielectric loss tangent  $\tan \delta$  from  $Q$ -factor data on MTL resonators, at an SFQ-logic operating temperature of liquid helium (LHe) of 4.2 K.

Resonant structures provide the most sensitive measurements of  $R_s$  [31–43] and  $\tan \delta$  [34,44–48] at microwave frequencies. We shall employ finite-length sections of MTL, with specified boundary conditions at the ends, to act as MTL resonators, enabling precise measurements of loss and inductance [49–51]. A resonator  $Q$  factor is defined as  $Q = 2\pi f_r W/P \gg 1$ , where  $f_r$  is the resonant frequency,  $W$  is the energy stored in the resonator, and  $P$  is the net power lost by the resonator [52]. In practice, one measures the

loaded  $Q$  factor

$$\frac{1}{Q_l} = \frac{1}{Q_i} + \frac{1}{Q_e} = \frac{1}{Q_c} + \frac{1}{Q_d} + \frac{1}{Q_r} + \frac{1}{Q_e},$$

where  $Q_i$  is the internal (unloaded)  $Q$  factor associated with the resonator intrinsic losses,  $Q_e$  is the external (coupling)  $Q$  factor associated with the resonator excitation, and  $Q_c$ ,  $Q_d$ , and  $Q_r$  are the partial  $Q$  factors associated with the conductor, dielectric, and radiation power loss, respectively. Besides the primary conductor and dielectric forming the resonator,  $Q_c$  and  $Q_d$  may include “extraneous” contributions from materials such as niobium oxides terminating the wall of the Nb cavity [23,53] or two-level systems (TLSs) residing at the dielectric surface and interface of superconducting quantum circuits [48,54–56]. The coupling contribution  $Q_e$  can be removed by the modern analysis techniques [57–59]. The radiation loss is often small and can be ignored [60,61]. Since  $Q_c^{-1}$  and  $Q_d^{-1}$  are additive, the conductor and dielectric loss contributions are inseparable. To deduce just one of them, the other loss must be either supposed or minimized by the resonator temperature, frequency, and/or geometry. The  $Q_c \ll Q_d$  regime favors the measurement of  $R_s$ , whereas the  $Q_d \ll Q_c$  regime favors the measurement of  $\tan \delta$ .

Cavity [32,33,37,38] and quasi-optical [40,61] resonators exploit the  $Q_c \ll Q_d$  regime, to measure  $R_s$  of bulk or thin-film superconductors. Klein *et al.* have proposed a copper pill-box cavity where the superconducting end plate contributes 40% of the net resistive loss at 86 GHz [62]. A superconducting dielectric resonator with  $Q_c \lesssim Q_d$  involves supposing  $\tan \delta$  for the dielectric rod, to deduce  $R_s$  of superconducting films [41,63]. Conversely, Krupka *et al.* have optimized a dielectric resonator for  $Q_d \ll Q_c$ , to measure  $\tan \delta$  of low-loss dielectrics [64] and high-resistivity silicon [65] at cryogenic temperatures. Kaiser has ignored the Nb loss in the lumped-element resonator with  $Q_d \ll Q_c$ , to investigate the frequency dependence of  $\tan \delta$  for amorphous thin-film dielectrics at 4.2 K [46]. Quantum computing circuit resonators exploit  $Q_d \ll Q_c$ , to characterize a TLS dielectric loss at millikelvin temperatures, where the superconductor loss is negligible [48,54–56,66]. Tuckerman *et al.* has exploited  $Q_d \ll Q_c$  to measure  $\tan \delta$  of Nb/polyimide flexible transmission-line tapes below 1.2 K [47]. At 3–4.2 K and 2–20 GHz, they observe both the dielectric and superconductor losses, extracting  $\tan \delta$  but not  $R_s$ . Golosovsky *et al.* have noted that at 4.3 K and 1.8 GHz, the losses in an Nb/Mylar microstrip resonator are dominated by the dielectric and radiation losses [67]. Likewise, Oates *et al.* have reported that at 4 K and 2.3–4.5 GHz, losses in Nb/SiO<sub>2</sub> submicron strip-line resonators are dominated by the dielectric loss, except for the narrowest strips [68]. However, the last two papers do not report  $\tan \delta$  or  $R_s$ . To overcome these limitations,

Taber has proposed to vary the dielectric spacer thickness (geometric factor) of the superconducting parallel-plate resonator, which allows the deduction of  $R_s$ ,  $\tan \delta$ , radiation loss [39] and the magnetic penetration depth  $\lambda$  [42,69]. However, this approach is impractical for interconnect characterization.

In contrast to existing work, we shall extract both the superconductor and dielectric losses by exploiting their frequency dependence in a multimode MTL resonator. In fact, we take advantage of both losses in our resonators being of comparable magnitude,  $Q_c \sim Q_d$ , owing to interplay between the loss and geometry. Fitting an analytical model to the experimental dependence of  $Q_i^{-1}$  on the resonant frequency, we quantitatively deconvolve  $R_s$  and  $\tan \delta$  in a single measurement.

The modeling of superconductor interconnects [28,70–74] has relied on the Leontovich boundary condition [75–77], often referred to as a surface-impedance boundary condition (SIBC) [78]. It approximates the transmitted wave as a wave propagating normal to the surface of an imperfect conductor, regardless of the incident angle. The SIBC is immensely fruitful for electrically large systems with a superconductor surface curvature radius much greater than the magnetic penetration depth  $\lambda$  [33,35,37,41–43,79]. However, the SIBC is inapplicable to deep-submicron interconnects with a wire cross section comparable to or smaller than  $\lambda \sim 100$  nm. To overcome this, we shall deal the intrinsic or wave impedance  $Z_s = R_s + iX_s = \sqrt{i\mu_0\omega/\sigma}$ , where  $R_s$  and  $X_s$  are the resistance and reactance,  $\mu_0$  is the vacuum permeability,  $\omega = 2\pi f$  is the angular frequency with  $f$  being the linear frequency,  $\sigma = \sigma_1 - i\sigma_2$  is the superconductor complex conductivity [80,81], and the time-harmonic convention is  $e^{i\omega t}$ . A good superconductor with  $\sigma_1 \ll \sigma_2$  or  $R_s \ll X_s$  has  $R_s = \omega^2 \mu_0^2 \lambda^3 \sigma_1(\omega)/2$  and  $X_s = \omega \mu_0 \lambda$ . Since, for a bulk conductor, the intrinsic and surface impedances are equal, we shall retain the  $R_s$  symbol for the *intrinsic* resistance.

To relate  $R_s$  and  $Q_c$ , and  $\tan \delta$  and  $Q_d$ , we shall define the respective conductor and dielectric geometric factors of a transmission-line resonator. The former is exclusively determined by the line cross-section geometry and  $\lambda$  and the latter is determined by the geometry and  $\epsilon_r$ . Involving fields and currents inside the conductor, the geometric factor calls for a three-dimensional (3D) finite-element method (FEM) capable of solving a superconductor interior [29,82]. Adapting the Ansys High Frequency Structure Simulator (HFSS) [83] to solve *inside* the superconductor, we shall overcome a limitation of the SIBC-based modeling [70–74] to interconnects with a much bigger cross section than  $\lambda$ . FEM can also address interconnects of complex geometry, including fabrication effects such as an irregular shape and rounded edges of the wire, mistargeting and variation of critical dimensions, intermixing of materials at the interface, dummy metal fill, etc. Combining HFSS modeling with focused-ion-beam (FIB) or

scanning-transmission-electron-microscopy (STEM) cross sectioning, we find the geometric factors of actual MTLs, to investigate  $R_s$  and  $\tan \delta$  as functions of the Nb wire width down to 0.25  $\mu\text{m}$ .

This paper is organized as follows. First, we will describe the design, fabrication, and characterization of a multimode MTL resonator. After presenting data for the frequency dependence of internal  $Q$  factor, we will derive a theoretical form to fit them. Next, the resonator geometric factors involved in the theory will be obtained using HFSS. Finally, the superconductor and dielectric losses will be deduced from the fit and their dependence on the MTL geometry and processing conditions will be scrutinized with the aid of a microscopic elemental analysis.

## II. RESONATOR DESIGN, FABRICATION, AND CHARACTERIZATION

### A. Design and layout

To implement the proposed concept, we have designed a chip with five half-wavelength open-circuited MTL resonators, as shown in Fig. 1(a). The MTL is formed by a Nb ground plane and conducting strip, embedded into TEOS-derived SiO<sub>2</sub>. The conducting-strip width  $w$  varies from 0.25 to 4  $\mu\text{m}$ , representative of RQL interconnects. Meandering the microstrip conserves space. The meander sections are spaced far apart (35  $\mu\text{m}$  center-to-center), to minimize the inductive coupling [84]. Via walls surround the conducting strip, as shown in Fig. 1(b). They are placed at least 15 times the dielectric thickness away from the conducting-strip edge, to minimize the near-field coupling and loss contribution to MTL.

A superconducting MTL supports a slow TM<sub>00</sub> wave [28,85,86], which is dispersionless up to 100 GHz for our geometries [29]. Solving a resonant condition  $\beta l_{\text{res}} = \pi n$  yields the resonator eigenfrequencies

$$f_n = \frac{n}{2l_{\text{res}}\sqrt{LC}} \approx \frac{nc}{2l_{\text{res}}\sqrt{\epsilon_r}} \sqrt{\frac{s}{s + 2\lambda \coth(d/\lambda)}}, \quad (1)$$

where  $\beta = 2\pi f \sqrt{LC}$  is the phase constant,  $L$  and  $C$  are the MTL series inductance and shunt capacitance per unit length, per Eqs. (A1b) and (A1d) in Appendix A,  $l_{\text{res}}$  is the resonator geometrical length,  $n = 1, 2, 3 \dots$  is the longitudinal mode index,  $c$  is the speed of light in vacuum,  $\epsilon_r$  is the relative dielectric constant,  $s$  is the dielectric spacing between the conducting strip and the ground plane, and  $d$  is the superconductor thickness. The approximation on the right of Eq. (1) is for wide microstrip with  $w \gg s$  (parallel-plate line) [42].

The resonator has been designed assuming the nominal fabrication thicknesses  $s = 150$  nm and  $d = 200$  nm, and the typical constitutive parameters  $\epsilon_r = 4.2$  for SiO<sub>2</sub> [87] and  $\lambda = 90$  nm for Nb. The latter has also been verified by superconducting quantum interference device

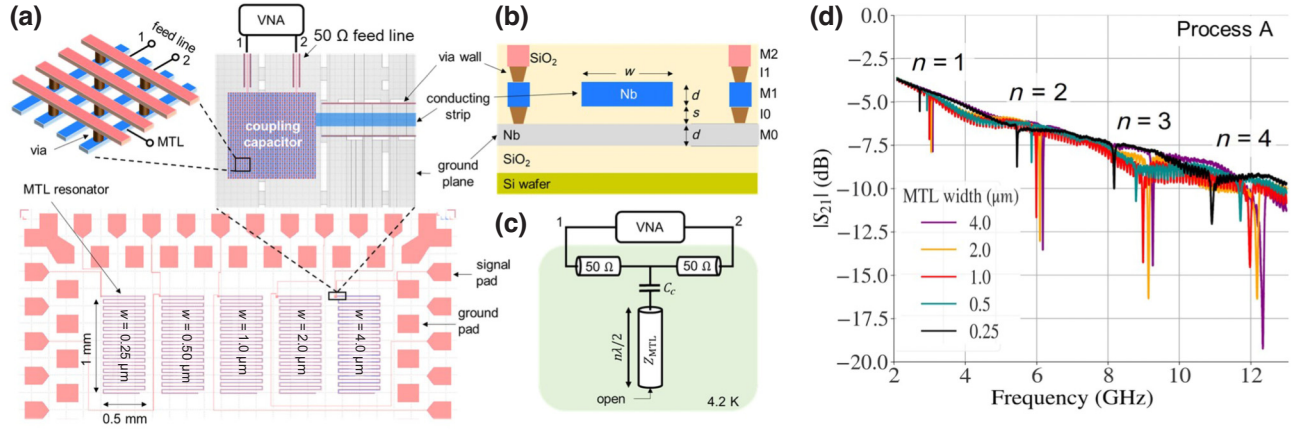


FIG. 1. (a) The chip layout, with five MTL resonators of conducting-strip width  $w$  varying from 0.25 to 4  $\mu\text{m}$ , fabricated by a three-metal-layer planarized process. Each resonator formed by meandering MTL takes up an area  $0.5 \times 1 \text{ mm}^2$  and is reactively coupled to a microstrip feed line running between two sets of ground-signal-ground contact pads. The enlargement shows the layout and 3D concept of a “plaid” coupling capacitor, formed by a crossbar array of wires sandwiching a rhombus grid of plug or stud vias. The capacitor connects the MTL resonator to a 50- $\Omega$  feed line conceptually connected to a vector network analyzer (VNA). (b) A diagram of the fabrication stack and MTL cross section for processes B or C (not to scale). The MTL is embedded in the dielectric. Via walls shield the conducting strip. M0 (gray), M1 (blue), and M2 (pink) are the Nb metal layers of thickness  $d = 200 \text{ nm}$ . I0 and I1 are the  $\text{SiO}_2$  interlayer dielectric layers of thickness  $s = 150 \text{ nm}$ , with Nb plug or stud vias (brown). Each layer is planarized and the stack is passivated with  $\text{SiN}_x$ . (c) A conceptual diagram of the resonator-excitation network. A coupling capacitor  $C_c$  connects the open-circuited half-wavelength resonator held at 4.2 K to the 50- $\Omega$  feed line. The VNA applies rf power and measures the complex transmission coefficient  $S_{21}$ . (d) Representative  $|S_{21}|$  spectra for five MTL resonators from a chip fabricated by process A. The resonant dips marked by the mode index  $n = 1$ –4 correspond to the first four  $\text{TM}_{00n}$  modes. The sloped background is due to loss in a cryogenic dip probe.

(SQUID) inductance measurements [88] and agrees with Ref. [17]. The selected resonator length  $l_{\text{res}} = 15 \text{ mm}$  is a trade-off between fitting many resonators on a  $5 \times 5 \text{ mm}^2$  chip and accommodating many resonant modes within the test-setup bandwidth. Equation (1) predicts a fundamental frequency  $f_1 = 3.27 \text{ GHz}$ , which agrees with the measured  $f_1 = 3.20 \pm 0.07 \text{ GHz}$  of a 4- $\mu\text{m}$ -wide resonator within 0.8%, justifying our assumed values for  $\epsilon_r$  and  $\lambda$ .

Figure 1(c) shows the resonator-excitation network. Each MTL resonator is reactively coupled to a microstrip feed line via a capacitor, shown in the enlargement in Fig. 1(a). We model this as a transmission line loaded by the shunt impedance  $Z_{sh}$  seen at the T-junction looking toward the coupling capacitor [14]. Such network has transmission coefficient  $S_{21} = 2Z_{sh}/(Z_0 + 2Z_{sh})$ , where  $Z_0 = 50 \Omega$  is the feed-line characteristic impedance. At resonance,  $Z_{sh} = R_{sh}$  is purely real and  $S_{21} = (1 + g)^{-1}$ , where  $g \equiv Q_i/Q_e$  is the resonator coupling coefficient [89], which leads to  $2R_{sh}/(Z_0 + 2R_{sh}) = (1 + g)^{-1}$ . Inserting here the input resistance for a capacitively coupled open-circuited half-wavelength microstrip resonator [52]  $R_{sh} = (8\pi f_n^2 C_c^2 Z_{MTL} Q_i)^{-1}$ , the resulting equation yields the coupling capacitance

$$C_c = \frac{1}{2f_n} \sqrt{\frac{g}{\pi Z_0 Z_{MTL} Q_i}}, \quad (2)$$

where  $Z_{MTL} = \sqrt{L/C}$  is the MTL characteristic impedance. To overcome the parasitic ripple in the transmission coefficient caused by impedance discontinuities in the measurement system [see Fig. 1(d)], we want about 6-dB insertion loss at a resonance. For the reactively coupled resonator, this corresponds to a critical coupling  $g = 1$  ( $R_{sh} = Z_0/2$ ). We evaluate  $Z_{MTL}$  and  $Q_i$  in Eq. (2) using the parallel-plate approximations of Eqs. (A1) and (B1a) in Appendices A and B. Assuming representative  $R_s = 2 \mu\Omega$  and  $\tan \delta = 10^{-3}$  at  $f_1$ , Eq. (2) results in a  $C_c$  of 50–250 fF for the MTL width of 0.25–4  $\mu\text{m}$ , respectively.

To implement such capacitors in a planarized process, where large metal patches are disallowed because of the CMP requirement to maintain the metal coverage density at about 50%, we have designed the “plaid” capacitor depicted in the enlargement in Fig. 1(a). It comprises a crossbar array of wires in two adjacent metal layers, M1 (blue) and M2 (pink), sandwiching a rhombus grid of vias in interlayer dielectric layer I1 (brown). The vias connect every other wire in M1 to every other wire in M2. This creates two interwoven electrodes of about the same capacitance per unit area as a parallel-plate capacitor.

## B. Fabrication

The MTL resonators have been fabricated by three generations of a three-metal-layer process with 0.25- $\mu\text{m}$



minimum feature size, referred to as *processes A, B, and C* below. In all of them, the Nb is made by physical vapor deposition and SiO<sub>2</sub> is made by plasma-enhanced chemical vapor deposition (PECVD) from a TEOS precursor. The latter has been done at lower temperature  $\lesssim 150^\circ\text{C}$  [90], to minimize the Nb contamination. Process A is a damascene process, using an inverted microstrip geometry with the ground plane on the M2 layer. Processes B and C are a damascene and a Cloisonné process, respectively, using a noninverted microstrip geometry with the ground plane on the M0 layer. Figure 1(b) represents the fabrication stack and the MTL cross section for processes B and C.

The damascene process begins with depositing a uniform layer of dielectric on a planarized surface. After the trenches or vias for interconnect wiring are defined by photolithography and subtractively patterned by reactive ion etching (RIE), a metal is deposited to fill and overfill (overburden) them. Finally, CMP removes the excess metal until the intermetal dielectric, embedding the wires or plug vias, is exposed. The surface is now smooth and ready for fabricating the next layer. To promote adhesion of SiO<sub>2</sub> to Nb, the planarized metal layer is treated with an oxygen plasma.

The Cloisonné process begins with depositing a uniform layer of metal on a planarized surface. After the interconnect wires or stud vias are defined by photolithography and subtractively patterned by RIE, a dielectric is deposited conformally over them. Once the metal features are completely embedded with dielectric, CMP removes the excess dielectric until the wires or vias are exposed. The surface is now smooth and ready for the next layer.

### C. Experimental

Figure 1(c) shows a conceptual diagram of the microwave test setup. Measurements have been taken at 4.2 K in a LHe Dewar using an rf dip probe equipped with a 32-contact-pad test fixture [14,26,27,29]. To avoid wire bonding and provide for fast sample exchange, a flip-chip press-contact technology is used, where the chip contact pads are pressed against nonmagnetic Cu-Au bumps in the fixture PCB, interfacing with the probe semirigid coaxial cables. A ground-signal-ground configuration facilitates isolation between the PCB traces. During the experiment, the fixture and the roughly 30 cm of the probe were immersed in a LHe bath. The complex transmission coefficient  $S_{21}$  was measured by a Keysight N5222A two-port vector network analyzer (VNA), calibrated to the top of the probe. To minimize the possibility of nonlinear effects [67,91,92], the microwave power in the chip feed line was kept below  $10\ \mu\text{W}$ .

Figure 1(d) shows the transmission-coefficient magnitude  $|S_{21}|$  versus the frequency for one of the chips made by process A. The signal fidelity limited the measurements to the first four modes  $n = 1\text{--}4$  of the MTL resonators. To extract the internal  $Q$  factor  $Q_i$  and resonant frequency  $f_n$  from the  $S_{21}$  data, we have employed a diameter-correction method (DCM) [57,58,93]. A critical resonator coupling  $g = 1$ , targeted in our design, minimizes the DCM circle fit error [59]. Depending on the process, the MTL width, and the mode index, we have observed  $Q_i$  between 170 and 700 and  $g$  from 0.1 to 3.8. The DCM fit error was found to be rather insensitive to the  $g$  value: 96% of the resonant peaks gave an error of  $< 1\%$ , while the rest gave an error of  $< 3\%$ . Reinserting the same chip several times into a test

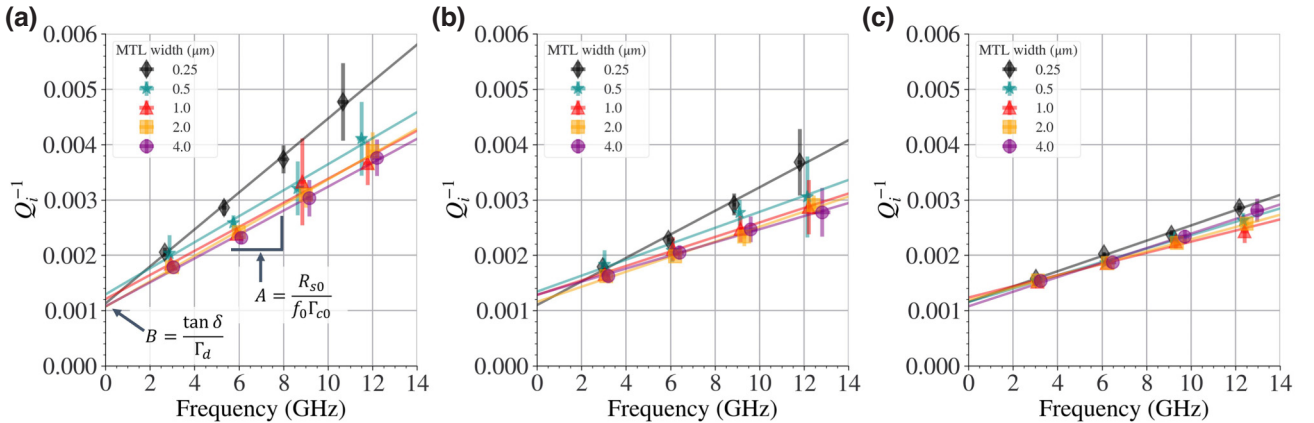


FIG. 2. The inverse internal  $Q$  factor  $Q_i^{-1}$  of the MTL resonators at 4.2 K versus the resonant frequency  $f_n$  for the first four modes  $n = 1\text{--}4$ . Each plot shows results for all five MTL widths  $w = 0.25\text{--}4\ \mu\text{m}$ , fabricated by (a) process A, (b) process B, and (c) process C.  $Q_i$  has been extracted from the  $S_{21}$  spectra as shown in Fig. 1(d). Each data point is the arithmetic mean for several chips per process. The solid lines are linear fits of Eq. (7) to the data for each MTL width fabricated by the respective process. The fit slope  $A$  is proportional to the intrinsic resistance  $R_s$  taken at a reference frequency  $f_0$  and the fit  $y$  intercept  $B = Q_i^{-1}$  is proportional to the dielectric loss tangent  $\tan \delta$  at gigahertz frequencies.  $\Gamma_c$  and  $\Gamma_d$  are the geometric factors associated with conductor and dielectric loss, respectively.

fixture gave the maximum spread in  $Q_i$  and  $f_n$  of less than 10% and 0.1%, respectively.

For each process, between six and nine chips were selected within the inner 80-mm diameter of the 150-mm wafer. Figure 2 shows data obtained from four wafers on a total of 22 chips (five resonators per chip). Each panel of Fig. 2 shows  $Q_i^{-1}$  as a function of the resonant frequency for all five MTL widths, for a particular fabrication process. Each data point and error bar represent the arithmetic mean and one standard deviation for a sample of six to nine chips per process, to statistically describe the loss variation for each MTL width for each process. The increased error bars for modes  $n = 3, 4$  in processes A and B are due to the parasitic ripple in  $S_{21}$  seen in Fig. 1(d).

### III. DATA-ANALYSIS METHOD

To explain the frequency dependence of  $Q_i^{-1}$  in Fig. 2, the transmission-line resonator geometric factor concept of Appendix A yields

$$Q_i^{-1} = \Gamma_c^{-1} R_s + \Gamma_d^{-1} \tan \delta, \quad (3)$$

where  $\Gamma_c$  and  $\Gamma_d$  are the geometric factors associated with the conductor and dielectric loss, respectively. The inverse quantities  $\Gamma_c^{-1}$  and  $\Gamma_d^{-1}$  are referred to as the filling or participation factors: the greater the filling factor, the more the material contributes to power loss. All quantities in Eq. (3) may depend on frequency. *A priori* assumptions about the frequency scaling will enable the fitting of Eq. (3) to the data of Fig. 2, to extract the superconductor and dielectric losses.

For low temperatures  $T < 0.5T_c$ , where  $T_c$  is the transition temperature, the Mattis-Bardeen microscopic theory [80] predicts  $\sigma_1(\omega) \propto \sinh(\hbar\omega/2k_B T) K_0(\hbar\omega/2k_B T)/\omega$ , where  $\hbar$  and  $k_B$  are the respective Plank and Boltzmann constants and  $K_0$  is the modified Bessel function [94]. At low frequencies  $\hbar\omega \ll 2k_B T$ , the above gives, for the Bardeen-Cooper-Schrieffer (BCS) surface resistance,  $R_{\text{BCS}}(\omega) \propto \omega^2 \ln(4k_B T/e^\gamma \hbar\omega)$ , where  $\gamma$  is Euler's constant [35,95]. At  $T = 4.2$  K, this holds up to 25 GHz, covering the (3–13)-GHz spectrum of our resonators. Then, ignoring the residual resistance compared to  $R_{\text{BCS}}$  at 4.2 K [35,37,96], an  $R_s$  frequency dependence can be approximated by

$$R_s = R_{s0} \left( \frac{\omega}{\omega_0} \right)^{2+a}, \quad (4)$$

where  $R_{s0} = R_s(\omega_0)$  is the intrinsic resistance taken at a reference frequency  $\omega_0$  and  $a = \ln[\ln(e^\gamma \hbar\omega/4k_B T) / \ln(e^\gamma \hbar\omega_0/4k_B T)] / \ln(\omega/\omega_0) \lesssim 0$  is the frequency-dependent deviation from a pure quadratic dependence  $R_s \propto \omega^2$  of the phenomenological two-fluid model. For representative  $\omega_0 = 2\pi \times 10$  GHz, the BCS theory predicts  $2 + a$  reducing from 1.75 to 1.6 over 1–13 GHz, at

4.2 K. In practice, smearing the singularity in the density of states (DOS) near an energy gap [97] removes the BCS divergence of  $\sigma_1(\omega)$  at  $\omega = 0$  [98], preserving  $a \approx 0$  in Eq. (4) into the gigahertz range [35]. This can be addressed by replacing  $k_B T/\hbar\omega \rightarrow k_B T/\gamma_D$  in the  $R_{\text{BCS}}(\omega)$  dependence [98], where a phenomenological Dynes parameter  $\gamma_D \ll \Delta$  quantifies the quasiparticle finite lifetime, where  $\Delta$  is the energy gap. For example, Bauer *et al.* have reported  $2 + a = 2 \pm 0.1$  over 1.7–7.8 GHz for a Nb cavity [96], whereas Philipp and Halbritter have found that  $2 + a$  reduces from 1.8 to 1.65 over 12–18 GHz, depending on Nb cavity oxidation [99]. Thus, the expected range of the frequency-scaling exponent in Eq. (4) is  $1.6 < 2 + a < 2.1$ .

A dielectric loss tangent can be expressed as  $\tan \delta = \sigma_d/\varepsilon_0 \varepsilon_r \omega$ , where  $\sigma_d$  is the material conductivity and  $\varepsilon_0$  is the vacuum permittivity [52]. According to Jonscher's universal relaxation law,  $\sigma_d$  scales with frequency as  $\sigma_d = \sigma_{dc} + F\omega^p$ , where  $\sigma_{dc}$  is the dc conductivity,  $F$  is the prefactor, and the exponent  $p$  falls in the range of  $0 < p \leq 1$  [100]. Thus, at high frequencies where  $\sigma_{dc} \ll F\omega^p$ , a  $\tan \delta$  frequency dependence can be approximated by

$$\tan \delta = \tan \delta_0 \left( \frac{\omega}{\omega_0} \right)^{p-1}, \quad (5)$$

where  $\tan \delta_0 = F\omega_0^{p-1}/\varepsilon_0 \varepsilon_r(\omega_0)$  is the loss tangent at a reference frequency  $\omega_0$ . Jonscher has proposed that low-loss dielectrics with  $\tan \delta < 0.1$  exhibit a nearly “flat loss” over several decades of frequency [100], corresponding to  $p \approx 1$  in Eq. (5). However, Kaiser has reported  $0.57 \leq p \leq 0.68$  for various amorphous thin-film dielectrics at 4.2 K and 0.1–20 GHz [46]. Conversely,  $\tan \delta$  of some low-loss crystals, ceramics, glasses, and polymers has been reported to increase linearly with frequency over 1–30 GHz at room temperature [44,101], corresponding to  $p = 2$ . Thus, the expected range of the frequency-scaling exponent in Eq. (5) is  $-1 < p - 1 \leq 1$ .

Concerning the geometric factors in Eq. (3), Eqs. (A5) of Appendix A infer that  $\Gamma_c \propto \omega$  while  $\Gamma_d$  is frequency independent. These rely on dispersionless  $\lambda$  and  $\varepsilon_r$ , as evidenced by the equidistant spectrum of resonant frequencies in Fig. 2. It then follows from Eqs. (3)–(5) that

$$\frac{1}{Q_i} = \frac{R_{s0}}{\Gamma_{c0}} \left( \frac{\omega}{\omega_0} \right)^{1+a} + \frac{\tan \delta_0}{\Gamma_d} \left( \frac{\omega}{\omega_0} \right)^{p-1}, \quad (6)$$

where the parameters subscripted with “0” are taken at a reference frequency  $\omega_0 = 2\pi f_0$ . We will choose  $f_0 = 10$  GHz within the resonator spectrum.

The nearly linear dependence of  $Q_i^{-1}$  on frequency in Fig. 2 can be interpreted as  $a \approx 0$  and  $p \approx 1$  in Eq. (6). The former supports a smearing of the DOS singularity in Nb, while the latter supports Jonscher's “flat loss” in SiO<sub>2</sub>.

According to the Kramers-Kronig relations, the “flat loss” coincides with dispersionless  $\varepsilon_r$  evidenced by the equidistant resonant-frequency spectrum. Such a dependence has also been observed by Tuckerman *et al.* for a Nb/polyimide multimode microstrip resonator at 3–4.2 K over 2–20 GHz [47]. Thus, setting  $a = 0$  and  $p = 1$  reduces Eq. (6) to the linear form

$$Q_i^{-1}(f) = \frac{R_{s0}f}{\Gamma_{c0}f_0} + \frac{\tan \delta}{\Gamma_d} = Af + B, \quad (7)$$

where  $A = R_{s0}/\Gamma_{c0}f_0$  and  $B = \tan \delta/\Gamma_d$ . Fitting Eq. (7) to the data sets in Fig. 2, with  $A$  and  $B$  as the fitting parameters, the fit slope  $A$  is proportional to  $R_{s0}$  and the fit  $y$  intercept  $B$  is proportional to  $\tan \delta$ . For instance, process A has a larger fit slope, and hence a higher superconductor loss, than processes B and C, for all MTL widths. For MTL width 1  $\mu\text{m}$  and under, process B has a higher superconductor loss than process C, while for the 2- and 4- $\mu\text{m}$ -wide MTLs, processes B and C have similar losses. All processes and line widths give roughly the same  $y$  intercept  $B \approx 0.0012$ , corresponding to  $Q_d \approx 830$ .

For an MTL with conducting-strip and ground-plane partial resistances  $R_s^{cs}$  and  $R_s^{gp}$ , Eq. (A3) of Appendix A gives, for the first addend in Eq. (3),

$$\overline{\frac{R_s}{\Gamma_c}} = \frac{R_s^{cs}}{\Gamma_c^{cs}} + \frac{R_s^{gp}}{\Gamma_c^{gp}}, \quad (8)$$

where  $\overline{R_s}$  is understood as an averaged quantity and  $\Gamma_c^{cs}$  and  $\Gamma_c^{gp}$  are the partial geometric factors associated with the conducting-strip and ground-plane resistive losses. Likewise, for an MTL with inhomogeneous dielectric per Fig. 1(b), Eq. (A3) gives, for the second addend in Eq. (3),

$$\overline{\frac{\tan \delta}{\Gamma_d}} = \frac{\tan \delta^{\text{Si}}}{\Gamma_d^{\text{Si}}} + \frac{\tan \delta^{\text{SiO}_2}}{\Gamma_d^{\text{SiO}_2}} + \frac{\tan \delta^{\text{SiN}}}{\Gamma_d^{\text{SiN}}} \approx \frac{\tan \delta^{\text{SiO}_2}}{\Gamma_d^{\text{SiO}_2}}, \quad (9)$$

where  $\overline{\tan \delta}$  is the averaged quantity and the partial loss tangents  $\tan \delta^\#$  and geometric factors  $\Gamma_d^\#$  are superscripted with the respective material, including an Si wafer substrate, an SiO<sub>2</sub> interlayer dielectric, and an SiN<sub>x</sub> passivation layer. Excluding the liquid helium from consideration makes  $\Gamma_d > 1$ . The approximation on the right of Eq. (9) ignores all the losses except for SiO<sub>2</sub>, exploiting  $\tan \delta^{\text{SiO}_2} \gg \tan \delta^{\text{Si}}$ ,  $\tan \delta^{\text{SiN}}$  [46] and  $\Gamma_d^{\text{SiO}_2} \ll \Gamma_d^{\text{Si}}$ ,  $\Gamma_d^{\text{SiN}}$ . Note that  $1/\Gamma_d^{\text{Si}} \approx 0$  for the inverted MTL of process A, and  $1/\Gamma_d^{\text{Si}} \approx 0$  for the noninverted MTL of processes B and C.

Fitting Eq. (7) to the data gives the Nb and SiO<sub>2</sub> losses as

$$R_{s0} = f_0 \Gamma_{c0} A, \quad (10a)$$

$$\tan \delta^{\text{SiO}_2} \approx \Gamma_d^{\text{SiO}_2} B, \quad (10b)$$

where Eq. (10b) follows from a general relation  $\tan \delta = \Gamma_d B$  using Eq. (9). For the wide MTL of  $w \gg s$ , the geometric factors in Eqs. (10) can be found from a parallel-plate approximation per Appendix B:

$$\Gamma_{c0PP} = \omega_0 \mu_0 \frac{s + 2\lambda \coth(d/\lambda)}{2 [\coth(d/\lambda) + (d/\lambda)/\sinh^2(d/\lambda)]}, \quad (11a)$$

$$\Gamma_{dPP}^{\text{SiO}_2} = 1. \quad (11b)$$

For the narrow MTL of  $w \lesssim s$ , finding  $\Gamma_{c0}$  and  $\Gamma_d$  requires FEM modeling, to account for the current concentration at the edges of the conducting strip [82,102], field fringing [103], and the irregular cross section of the conducting strip [104].

#### IV. HFSS MODELING

One can find geometric factors by numerically integrating Eqs. (A5) of Appendix A, which involve the fields and currents *inside* a superconductor. Sheen *et al.* is the only work to simulate these, in a superconducting strip line, using a proprietary FEM solver [82]. We employ the Ansys HFSS software [83] to extract geometric factors from the solved network parameters, circumventing the integration. HFSS is a full 3D FEM simulator, capable of solving fields, currents, and network parameters for an arbitrary electromagnetic structure. However, HFSS neither includes a lossy superconductor *material* nor allows superconducting ports [105]. Thus, the peculiar aspects of modeling a superconductor network in HFSS are (i) defining the lossy superconductor by a negative permittivity and a real conductivity [81]; (ii) using perfect electric conductor (PEC) to connect superconductor members to the excitation ports; and (iii) enforcing the *solve-inside* option for the superconductor members, to override the HFSS default of only solving inside a material when the conductivity  $< 10^5$  S/m.

##### A. Defining a superconductor in HFSS

Inserting the superconductor local current-field constitutive relation  $\mathbf{J} = (\sigma_1 - i\sigma_2)\mathbf{E}$  into Maxwell’s curl- $H$  equation gives

$$\nabla \times \mathbf{H} = \sigma_1 \mathbf{E} + i\omega \varepsilon_0 \left( \varepsilon - \frac{\sigma_2}{\varepsilon_0 \omega} \right) \mathbf{E},$$

where the parentheses enclose a superconductor relative permittivity  $\varepsilon_{sc} = \varepsilon - (\sigma_2/\varepsilon_0\omega)$ , in which  $\varepsilon$  is the ordinary dielectric constant associated with the displacement current. The superconductor is modeled as a collisionless electron plasma with the dielectric function  $\varepsilon_p = 1 - (\omega_p/\omega)^2 = 1 - (c/\omega\lambda)^2$ , where  $\omega_p = c/\lambda$  is the plasma frequency of the superfluid electrons [81,106,107] and the ionic contribution is ignored. Comparing  $\varepsilon_{sc}$  and  $\varepsilon_p$  infers that  $\varepsilon = 1$  is the permittivity in the limit  $\omega \gg \omega_p$  and  $\sigma_2 = 1/\omega\mu_0\lambda^2$  is the London conductivity. Therefore, a lossy superconductor can be defined as a material with the permittivity  $\varepsilon_{sc} = 1 - (\sigma_2/\varepsilon_0\omega)$  and conductivity  $\sigma_{sc} = \sigma_1$ , applicable over the entire range of temperatures and frequencies of interest. Ignoring the displacement current due to  $\sigma_2/\varepsilon_0\omega \gg 1$ , a superconductor permittivity is substantially a negative quantity  $\varepsilon_{sc} = -\sigma_2/\varepsilon_0\omega$  [108,109].

In Ref. [29], the authors have implemented a superconductor *material* in HFSS using the Mattis-Bardn theory to define  $\varepsilon_{sc}$  and  $\sigma_{sc}$  as piece-wise functions of frequency [29]. Here, we define them analytically, exploiting  $\sigma_1 \ll \sigma_2$ . Modeling  $\sigma_2$  as the London conductivity gives  $\varepsilon_{sc}^{\text{HFSS}} = -(c/\omega\lambda)^2$ , where  $\lambda$  is the experimental penetration depth. A two-fluid model gives  $\sigma_{sc}^{\text{HFSS}} = 2R_{s0}/\omega_0^2\mu_0^2\lambda^3$ , where  $R_{s0}$  is the experimental intrinsic resistance at a reference frequency  $\omega_0$ . These implicitly produce  $R_s^{\text{HFSS}} \propto \omega^2$ , to agree with Fig. 2 and Eq. (7).

## B. Modeling a superconducting MTL in HFSS

The MTL resonators in Fig. 1(a) exceed the HFSS limit of  $10^4$  for the ratio of the model largest to smallest dimension. Moreover, to solve inside a superconductor *material* with very high conductivity  $\sigma_{sc} \sim 10^7\text{S/m}$  and permittivity  $|\varepsilon_{sc}| \sim 10^9$ , FEM creates a very-high-density mesh, making very large structures prohibitively long to simulate. To overcome these limitations and determine  $\Gamma_c$  and  $\Gamma_d$ , we simply model a small longitudinal segment of uniform MTL, at a reference frequency  $f_0 = 10\text{ GHz}$ . Figure 3(a) shows the HFSS model of a two-port network formed by a superconducting microstrip, with PEC ports of the same cross-section geometry [29]. The superconducting MTL segment of length  $l = 5\text{--}20\ \mu\text{m}$  is electrically short  $\beta l \ll 1$ . The PEC port length  $l_{pec} = 1\ \mu\text{m}$  is a small fraction of  $l$ . After solving the model with the *terminal network-analysis* solution type [83], PEC ports are deembedded, to extract the network parameters of the MTL segment only.

Figure 3(b) shows the magnetic field intensity looking into the MTL cross section, for all five MTL widths, in the case of the nominal geometry and material parameters for processes B or C. For a 2- $\mu\text{m}$ -wide MTL and above, the magnetic field has a parallel-plate-like distribution. For 1  $\mu\text{m}$  MTL and below, the magnetic field penetrates the majority of the conducting strip but only a small fraction of the ground plane.

To provide accurate results, the HFSS convergence criterion has been set at 0.1–1% for the telegrapher's RLCG parameters  $R = \text{Re}(Z)$ ,  $L = \text{Im}(Z)/\omega$ ,  $G = \text{Re}(Y)$ , and  $C = \text{Im}(Y)/\omega$  [110], where  $Z$  and  $Y$  are the series impedance and the shunt admittance of a general transmission line [111]. For the electrically short network, Appendix C gives the following approximations:

$$Z \approx 2(Z_{11} - Z_{12})l^{-1}, \quad (12a)$$

$$Y \approx Z_{12}^{-1}l^{-1}, \quad (12b)$$

where  $Z_{11} = Z_{22}$  and  $Z_{12} = Z_{21}$  are the elements of the  $Z$ -parameter matrix solved by HFSS. All geometries and material definitions have been parametrized and swept using the OPTIMETRICS option [83]. It is tractable to complete about 100 parametric sweeps in a few hours. The use of an SIBC for the MTL ground plane can speed up the simulations.

## C. Extracting geometric factors from HFSS

To extract the conductor and dielectric geometric factors from the HFSS solution, recall that  $Q_c = \omega L/R$  and  $Q_d = \omega C/G$  for a transmission-line resonator [52]. Then, combining Eqs. (3) and (12) yields

$$\Gamma_{c0} = R_{s0}^{\text{HFSS}} \frac{\text{Im}(Z_{11} - Z_{12})}{\text{Re}(Z_{11} - Z_{12})}, \quad (13a)$$

$$\Gamma_d = \tan \delta^{\text{HFSS}} \frac{\text{Im}(Z_{12}^{-1})}{\text{Re}(Z_{12}^{-1})}, \quad (13b)$$

where  $R_{s0}^{\text{HFSS}} = \omega_0^2\mu_0^2\lambda^3\sigma_{sc}^{\text{HFSS}}/2$  is the intrinsic microwave resistance corresponding to the HFSS superconductor material definitions and  $\tan \delta^{\text{HFSS}}$  is the HFSS defined dielectric loss tangent. The partial geometric factor of just the conducting strip  $\Gamma_{c0}^{\text{cs}}$  is obtained by setting the ground-plane loss to zero in the HFSS model and vice versa for the ground-plane partial geometric factor  $\Gamma_{c0}^{\text{gp}}$ . Likewise, the partial geometric factor  $\Gamma_d^{\text{SiO}_2}$  of just  $\text{SiO}_2$  is obtained by setting all other dielectric losses to zero in the HFSS model. A geometric factor concept substantially accelerates the data analysis: each MTL geometry requires only a single HFSS simulation, using *any* conductivity  $\sigma_{sc}^{\text{HFSS}} \ll \omega_0\varepsilon_0\varepsilon_{sc}^{\text{HFSS}}$  (resistance  $R_{s0}^{\text{HFSS}} \ll \omega_0\mu_0\lambda$ ), and *any* loss tangent  $\tan \delta^{\text{HFSS}} \ll 1$ .

Figure 3(c) shows the net conductor geometric factor  $\Gamma_{c0} = (1/\Gamma_{c0}^{\text{gp}} + 1/\Gamma_{c0}^{\text{cs}})^{-1}$  and the partial geometric factor ratio  $\Gamma_{c0}^{\text{cs}}/\Gamma_{c0}^{\text{gp}}$  versus the MTL width, for nominal and actual MTL geometry, for all three processes. Both quantities decrease with the MTL width. For instance, the conducting-strip participation in the MTL net resistive loss increases from 57% for the 4- $\mu\text{m}$ -wide MTL to 85% for the 0.25- $\mu\text{m}$ -wide MTL. The simulated  $\Gamma_{c0}$  has been verified to be independent of  $R_{s0}^{\text{HFSS}}$  over 0.1–100  $\mu\Omega$ . The



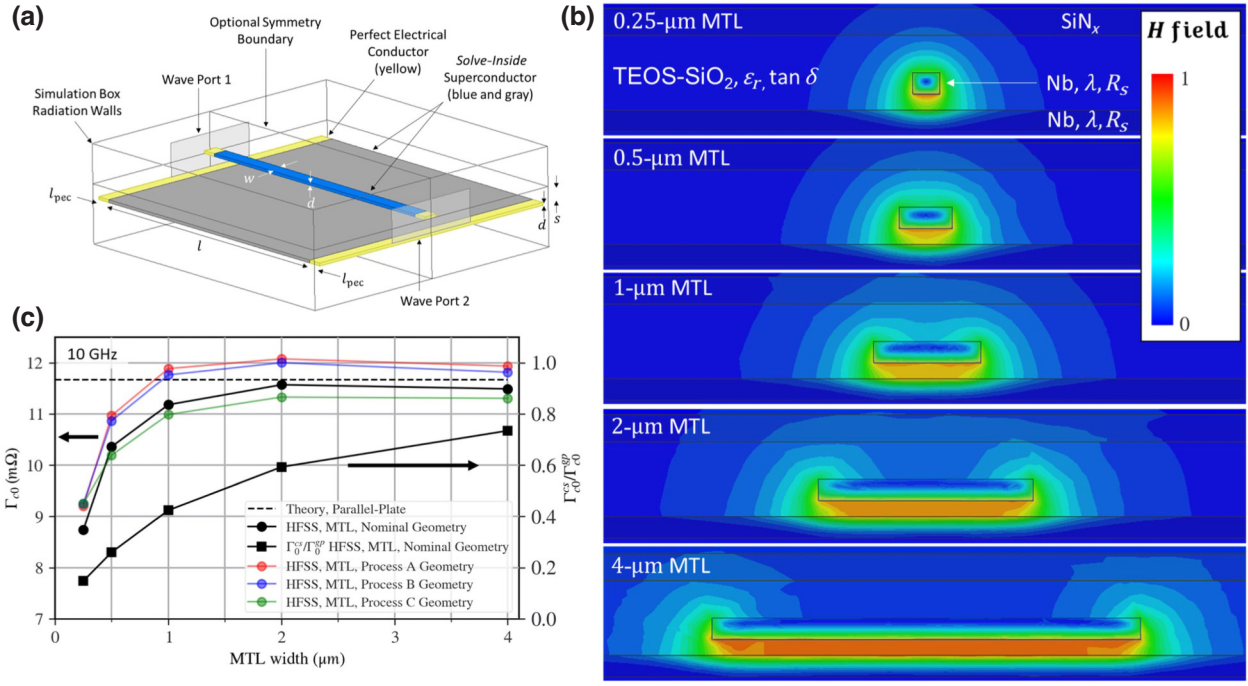


FIG. 3. (a) The HFSS model of a superconducting MTL. A dielectric (transparent) embeds a conducting strip (blue) of width  $w$  and a ground plane (gray), separated by the spacing  $s$ . Both conductors have thickness  $d$  and simulation length  $l$ . The MTL is enclosed by a simulation box with all faces set as *radiation* boundaries. To excite the model, PEC members (yellow) of length  $l_{pec}$  connect the wave ports to the superconductor members. (b) The magnetic field intensity looking into MTL cross section, simulated at 10 GHz. The MTL width varies from 0.25 to 4  $\mu\text{m}$ , top to bottom. Here,  $s = 150$  nm,  $d = 200$  nm, the Nb penetration depth and intrinsic resistance are  $\lambda = 90$  nm and  $R_s = 20$   $\mu\Omega$ , the SiO<sub>2</sub> relative dielectric constant and loss tangent are 4.2 and  $10^{-3}$ , respectively, and the SiN<sub>x</sub> relative dielectric constant and loss tangent are 7.5 and  $10^{-4}$ , respectively. (c) The conductor geometric factor  $\Gamma_{c0}$  at 10 GHz versus the MTL width, found from Eq. (13a) for the nominal cross-section geometry (black circles) and for the fabricated geometries for all three processes (red, green, and blue circles). The dashed black line is a parallel-plate approximation using Eq. (11a). The black squares show the conducting-strip to ground-plane geometric factor ratio  $\Gamma_{c0}^{cs}/\Gamma_{c0}^{gp}$ . The solid lines are a guide to the eye.

HFSS results have been further validated by comparing  $\Gamma_{c0}$  to the parallel-plate approximation given in Eq. (11a). For the nominal MTL geometry,  $\Gamma_{c0}$  (black solid line) approaches  $\Gamma_{c0PP}$  (black dashed line) within 1.5% at 2- $\mu\text{m}$  MTL width and above. This is evidenced by Fig. 3(b), where the fringing fields above the conducting strip segregate near the edges for 2- $\mu\text{m}$  width and above. Hence Eqs. (11) can be used for preliminary data analysis in wide MTLs with  $w/s > 13$ .

The HFSS simulations also show that, depending on the process, the dielectric geometric factor  $\Gamma_d^{\text{SiO}_2}$  increases from about 1.02 to 1.04 as the MTL width decreases. Such  $\Gamma_d^{\text{SiO}_2} \gtrsim 1$  is justified for an MTL embedded into mostly SiO<sub>2</sub> and agrees with Eq. (11b) for the wide MTL. Thus, the  $y$  intercept of linear fits in Fig. 2 nearly equals  $\tan\delta^{\text{SiO}_2}$ .

Solving just a short segment of the MTL, our HFSS model ignores the meandering of the microstrip on a chip. The nonmitered right-angle bend and inductive coupling between the long parallel sections reduce the inductance, whereas inductive coupling between the short collinear sections increases the inductance [84]. It is intuitively clear that a bend reduces both the inductance and resistance,

maintaining their ratio at nearly the same value. Consider a quarter-period-long segment of meander with a bend. The bend makes the conducting strip effectively wider by  $\Delta w \sim w^2/l_1$ , where  $l_1 \approx 250$   $\mu\text{m}$  is the segment geometric length. By Fig. 3(c), the increase in the geometric factor is  $\Delta\Gamma_{c0} \sim (\partial\Gamma_{c0}/\partial w)\Delta w$ , giving  $\Delta\Gamma_{c0}/\Gamma_{c0} < 1\%$  for all widths. The inductive coupling can be ignored due to a very large spacing  $\gg w, s, d$  between the adjacent meander sections and the via walls surrounding the conducting strip.

## V. RESULTS AND DISCUSSION

The cross-section geometries for each process and MTL width were measured by FIB or STEM. These actual geometries, including the slanted sidewalls of the conducting strip, were modeled in HFSS to find the geometric factors using Eqs. (13). Finally, such actual geometric factors were utilized to deduce the Nb averaged intrinsic resistance  $R_{s0}$  and the SiO<sub>2</sub> loss tangent  $\tan\delta^{\text{SiO}_2}$  from the linear fits in Fig. 2 using Eqs. (10).

Figure 4 shows the results versus the MTL width. The error bars are obtained by applying the error-propagation

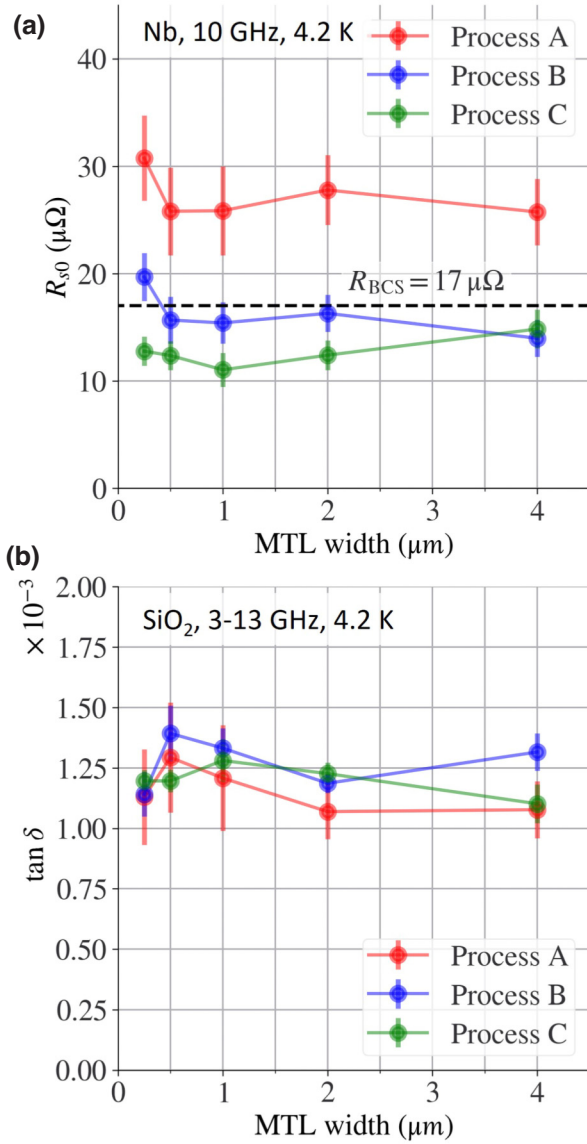


FIG. 4. (a) The Nb averaged intrinsic resistance per Eq. (8) at 4.2 K and 10 GHz versus the conducting-strip width and fabrication process, deduced from the fit slope in Fig. 2 using Eq. (10a). The black dashed line represents the minimal theoretical BCS surface resistance  $R_{BCS} \approx 17 \mu\Omega$  [96,112]. (b) The  $\text{SiO}_2$  dielectric loss tangent at 4.2 K and gigahertz frequencies versus the line width and fabrication process, deduced from the fit  $y$  intercept in Fig. 2 using Eq. (10b). The solid lines in both plots are a guide to the eye.

analysis to Eqs. (10), neglecting correlations. The uncertainties in the fit slope  $A$  and  $y$  intercept  $B$  are estimated from the linear regression in Fig. 2. The uncertainties in  $\Gamma_c$  and  $\Gamma_d$  are found using HFSS to model the effects of MTL-geometry variations across the wafer [110].

Figure 4(a) reveals that the Nb resistive loss decreases from process A to process B to process C. To compare the process-C  $R_{s0} \approx 13 \mu\Omega$  to the literature, we use  $R_s \propto$

$f^2$ . Scaling  $13 \mu\Omega$  to the dielectric resonator frequency 27.5 GHz gives  $100 \mu\Omega$ , which is 23% below a  $130\text{-}\mu\Omega$  surface  $R_s$  reported for 200-nm-thick Nb thin films at 4.2 K [63]. Scaling  $13 \mu\Omega$  to the parallel-plate resonator frequency 12.5 GHz gives  $20 \mu\Omega$ , which is 13% below a  $23\text{-}\mu\Omega$  surface  $R_s$  reported for 350-nm-thick sputtered Nb films at 4.2 K [39]. Scaling  $13 \mu\Omega$  to the cavity-resonator frequency of 1.5 GHz gives  $290 \text{ n}\Omega$ , which is 21% below a BCS surface resistance  $R_{BCS} = 365 \text{ n}\Omega$  reported for 1.5- $\mu\text{m}$ -thick Nb film on Cu backing at 4.2 K [37]. Remarkably,  $13 \mu\Omega$  is also 24% below a minimum theoretical  $R_{BCS} \approx 17 \mu\Omega$  predicted for Nb with the optimum mean free path at 10 GHz and 4.2 K [96,112]. This can be attributed to the DOS smearing [98,99], which is consistent with the quadratic frequency dependence of  $R_s$  implied by Fig. 2. We note that if the *actual* frequency dependence of the resistive loss is weaker than quadratic, fitting the Fig. 2 data with Eq. (7) may slightly underestimate  $R_{s0}$ . A presumed  $\lambda$  value could be another source of systematic error: however, a 10% error in  $\lambda$  only produces an approximately 2% error in  $\Gamma_c$  and so  $R_{s0}$ . Thus, processes B and C demonstrate that planarized Nb interconnects can be scaled down to deep-submicron dimensions with minimal resistive loss.

Figure 4(b) shows that all three processes yield approximately the same  $\text{SiO}_2$  loss tangent  $\tan \delta \approx 0.0012$ , roughly independent of the MTL width. Such a value corroborates Oates *et al.*, who have reported  $Q \sim 600$  for submicron Nb/ $\text{SiO}_2$  strip-line resonators at 4 K and 2.3–4.5 GHz [68], which implies  $\tan \delta < 0.0016$  for a (200–300)-nm-thick planarized PECVD  $\text{SiO}_2$ . Our result also compares to Kaiser [46], who have reported  $\tan \delta = 0.0003\text{--}0.0007$  for sputtered  $\text{SiO}_2$  films over 1–9 GHz at 4.2 K. Note that depending on the *actual* frequency dependence of Nb  $R_s$ , fitting Eq. (7) to the data may slightly overestimate  $\tan \delta$ . Thus, the  $\text{SiO}_2$  loss is not sensitive to significant differences between the three processes, permitting a large fabrication window.

According to Eq. (3), a resonator optimized for characterization of both superconductor and dielectric loss has  $\Gamma_c^{-1}R_s = \Gamma_d^{-1}\tan \delta$ . The optimum geometric factor ratio  $r = \Gamma_c/\Gamma_d$  is then  $r^* = R_s/\tan \delta$ . The representative  $R_s \sim 20 \mu\Omega$  and  $\tan \delta \sim 10^{-3}$  of Fig. 4 call for  $r^* \sim 20 \text{ m}\Omega$ . At the same time, for the fabrication stack in Fig. 1(b), Eqs. (11) and Fig. 3(c) give  $r \sim 10 \text{ m}\Omega$ , comparable to  $r^*$ . Thus, our resonators are sensitive to both types of loss.

### A. $R_{s0}$ variation with process

To understand the Nb resistive loss variation with process seen in Fig. 4(a), we have performed a STEM analysis complemented by an EDS mapping on the 0.25- and 1- $\mu\text{m}$  wide MTLs, for all three processes. The electron beam was 0.1–1 nm in diameter and the detection limit was  $> 1$  at.%. Figures 5(a)–5(c) show representative STEM cross sections of the conducting strip looking into the

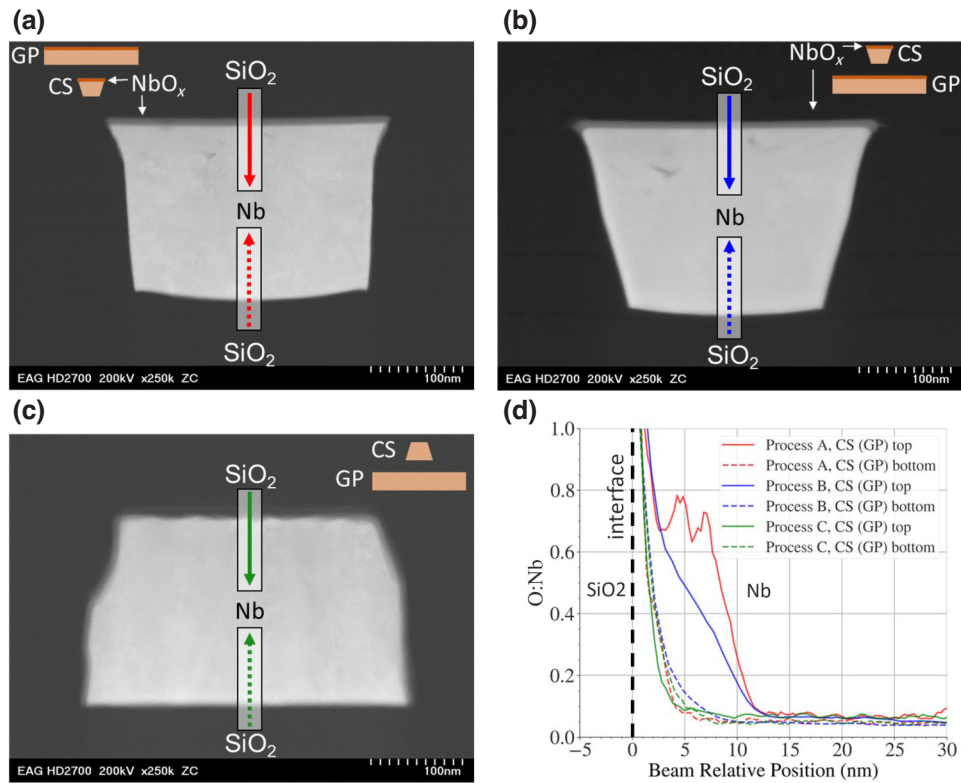


FIG. 5. STEM cross sections of the conducting strip for representative 0.25- $\mu\text{m}$  MTL resonators fabricated by (a) process A, (b) process B, and (c) process C. The sketches depict corresponding MTL cross sections, showing NbO<sub>x</sub>-layer locations in both the conducting strip (CS) and the ground plane (GP). (d) EDS profiles of the O:Nb content ratio just below the Nb surface as a function of the electron-beam relative position, corresponding to line cuts shown by the colored arrows in (a)–(c). The zero-beam position is set at the SiO<sub>2</sub>-Nb interface. The MTL ground plane is assumed to have the same O:Nb profile as the respective conducting strip.

0.25- $\mu\text{m}$ -wide MTL, for all three processes. The STEM and FIB cross sections reveal that processes A and B have a 10-nm-thick layer of oxidized Nb (NbO<sub>x</sub>) on the top of both the conducting strip and the ground plane, due to the oxygen-plasma treatment. Process C has no visible NbO<sub>x</sub> layers.

Oxidation can degrade Nb superconductivity by creating, in an inward direction, insulating niobium pentoxide (Nb<sub>2</sub>O<sub>5</sub>), semiconducting niobium dioxide (NbO<sub>2</sub>), metallic or superconducting niobium monoxide (NbO), and clustered or interstitially dissolved O [23,53,99,113]. Figure 5(d) shows EDS profiles for the O:Nb content ratio near the top and bottom faces of a 0.25- $\mu\text{m}$ -wide conducting strip, for all three processes. Comparison of EDS maps for 0.25- $\mu\text{m}$  and 1- $\mu\text{m}$  conducting strips suggest that all widths have a similar O:Nb profile. At the time of EDS data collection, it was deemed that only the conducting strip was of interest, so the ground-plane mapping was not performed. However, since it is created by the same deposition recipe, the ground plane likely incurs the same O:Nb profile as the respective conducting strip. This is supported by the FIB cross section of the entire MTL, which reveals that NbO<sub>x</sub> has the same thickness in both the ground plane

and the conducting strip, for all MTL widths. Hence, the plot legend in Fig. 5(d) itemizes the ground-plane O:Nb profile, inferred from the respective conducting strip, in parentheses.

Figure 3(b) demonstrates that the majority of the rf current flows near the ground-plane and conducting-strip surfaces facing each other and the strip corners next to the ground plane [82]. Hence, the O content in these regions may affect the MTL resistive loss. Figure 5(d) reveals that for process A, O extends about 10 nm into the top of the conducting strip but diminishes within just a few nanometers into the bottom of the ground plane; the O content overlaps with the current-density peaks at the strip corners, due to an inverted microstrip geometry. For process B, O extends about 10 nm into the ground-plane top but diminishes within a few nanometers into the conducting-strip bottom; the O content does not overlap with the current-density peaks at the strip corners. For process C, O diminishes within a few nanometers into both the ground-plane top and the conducting-strip bottom. For process A, the O:Nb ratio shows a hump around 4–8 nm into the conducting-strip top. These observations are consistent with the about 2 times difference in  $R_{s0}$  between



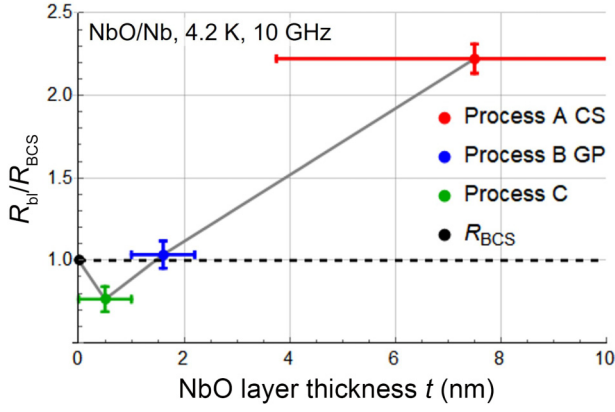


FIG. 6. The NbO/Nb bilayer microwave resistance  $R_{bl}$ , normalized by  $R_{BCS}$ , as a function of the NbO-layer thickness using the process-A conducting strip (CS), the process-B ground plane (GP), and process C. The black dashed line and the solid symbol at  $t = 0$  represent a theoretical BCS resistance  $R_{BCS} \approx 17 \mu\Omega$  for pristine Nb [112] using the parameters of Ref. [96]. The gray solid line is a guide to the eye. Large error bars represent estimated values for the thickness.

processes A and B, as well as with process C having a lower  $R_{s0}$  than process B. Considering that  $R_{s0} < R_{BCS}$  for process C, neither SiO<sub>2</sub> PECVD nor REI nor CMP degrade the Nb resistive loss, despite RIE causing the rough surface of the conducting strip [see Figs. 7(c) and 7(d)]. This makes a planarized Cloissonné process very attractive for fabricating low-loss Nb interconnects.

Figure 4 allows one to evaluate a partial loss associated with the NbO<sub>x</sub> layer. First, assume that the entire layer is insulating, e.g., Nb<sub>2</sub>O<sub>5</sub>. Since the measured  $\tan \delta$  is roughly independent of the MTL width, consider a wide MTL. Modeling the dielectric spacer as two parallel-plate capacitors filled with SiO<sub>2</sub> and Nb<sub>2</sub>O<sub>5</sub>, and connected in series, gives the averaged loss

$$\tan \delta = \frac{\tan \delta^{\text{SiO}_2} \epsilon_r^{\text{Nb}_2\text{O}_5} s + \tan \delta^{\text{Nb}_2\text{O}_5} \epsilon_r^{\text{SiO}_2} t}{\epsilon_r^{\text{Nb}_2\text{O}_5} s + \epsilon_r^{\text{SiO}_2} t}, \quad (14)$$

where  $\epsilon_r^{\text{Nb}_2\text{O}_5}$ ,  $\tan \delta^{\text{Nb}_2\text{O}_5}$ , and  $t$  are the dielectric constant, loss tangent, and thickness of the Nb<sub>2</sub>O<sub>5</sub> layer,  $\epsilon_r^{\text{SiO}_2}$  is the SiO<sub>2</sub> dielectric constant, and it is assumed that  $\tan \delta^{\text{Nb}_2\text{O}_5}, \tan \delta^{\text{SiO}_2} \ll 1$ . Using  $\epsilon_r^{\text{SiO}_2} t \ll \epsilon_r^{\text{Nb}_2\text{O}_5} s$  due to  $\epsilon_r^{\text{Nb}_2\text{O}_5} \sim 33$  [46], Eq. (14) reduces to

$$\tan \delta \approx \tan \delta^{\text{SiO}_2} + \frac{\epsilon_r^{\text{SiO}_2} t}{\epsilon_r^{\text{Nb}_2\text{O}_5} s} \tan \delta^{\text{Nb}_2\text{O}_5}, \quad (15)$$

where the participation factor  $\epsilon_r^{\text{SiO}_2} t / \epsilon_r^{\text{Nb}_2\text{O}_5} s \sim 0.01$  for  $t = 10$  nm and  $s = 150$  nm. Thus, the MTL resonator is rather insensitive to the Nb<sub>2</sub>O<sub>5</sub> loss. Assuming 10% measurement sensitivity and  $\tan \delta^{\text{SiO}_2} = 10^{-3}$  infers  $\tan \delta^{\text{Nb}_2\text{O}_5} \leq 0.01$  as an upper bound. This agrees with

Kaiser, who reports  $\tan \delta = 0.002\text{--}0.001$  for a thin-film Nb<sub>2</sub>O<sub>5</sub> made by Nb anodizing, over 1–15 GHz at 4.2 K [46]. Thus, the NbO<sub>x</sub> layer in processes A and B could be comprised of Nb<sub>2</sub>O<sub>5</sub>.

To resolve the difference in resistive loss between processes A and B of Fig. 4(a), now assume that the NbO<sub>x</sub> layer is metallic, e.g., NbO, which becomes a superconductor below 1.4 K [114]. Since the measured  $R_{s0}$  is roughly independent of the MTL width, consider a wide MTL subject to the SIBC and ignore the host finite-thickness effects due to  $d > 2\lambda$ . Modeling the oxidized Nb as a normal-metal/superconductor (N/S) bilayer gives the surface resistance [115,116]

$$R_{bl} = \omega^2 \mu_0^2 (\lambda_h + t)^2 t \sigma_n + R_h, \quad (16)$$

where  $t$  and  $\sigma_n$  are the N-layer thickness and normal conductivity,  $\lambda_h$  and  $R_h$  are the S-host penetration depth and surface resistance, and proximity coupling [117] between the N and S regions is ignored. It is also assumed that  $t$  is small enough to provide a uniform superfluid density in the N layer, in the case of the proximity coupling. The first addend, representing an N-layer contribution, has quadratic frequency dependence, which is consistent with Fig. 2 and Eq. (7). A term in parentheses,  $\lambda_{bl} = \lambda_h + t$ , represents the bilayer global penetration depth, as the decoupled N layer provides no screening [115]. In practice, proximity coupling makes  $\lambda_h \lesssim \lambda_{bl} < \lambda_h + t$ , which justifies using the same  $\lambda$  in the HFSS modeling of all processes.

Created by the same Nb-deposition recipe as process C, the process-A ground plane and the process-B conducting strip should have the same partial resistance of 13  $\mu\Omega$ , as the damascene effects are negligible for line widths  $w \gg d$  (see Sec. VB). Taking 27  $\mu\Omega$  and 15  $\mu\Omega$  for the averaged  $R_{s0}$  of processes A and B per Fig. 4(a) and using geometric factors per Fig. 3(c), Eq. (8) thus yields  $R_s^{\text{CS}} = 38 \mu\Omega$  and  $R_s^{\text{GP}} = 18 \mu\Omega$  for the process-A conducting strip and the process-B ground plane, respectively. Considering these as  $R_{bl}$ , using  $\omega = 2\pi \times 10$  GHz,  $\lambda_h = 90$  nm,  $t = 10$  nm, and again assuming that  $R_h = 13 \mu\Omega$  per process C, Eq. (16) yields  $\sigma_n = 4.0 \times 10^7$  S/m and  $\sigma_n = 7.4 \times 10^6$  S/m for the respective N layers of processes A and B. The former is remarkably close to the conductivity of  $5.56 \times 10^7$  S/m for an as-cast NbO alloy at 4.2 K [114]. Both N-layer conductivities being lower than this, however, infer that the NbO layer comprises only a fraction of the NbO<sub>x</sub> layer, which is consistent with NbO typically residing between a Nb host and higher oxides [23,53,99,113]. Then, inserting  $\sigma_n = 5.56 \times 10^7$  S/m into Eq. (16) and solving for the thickness gives  $t \approx 7.5$  nm and  $t \approx 1.6$  nm for the respective N layers of processes A and B, which agrees with Fig. 5(d). Thus, a 2 times difference in the resistive loss between processes A and B can be attributed to a 5



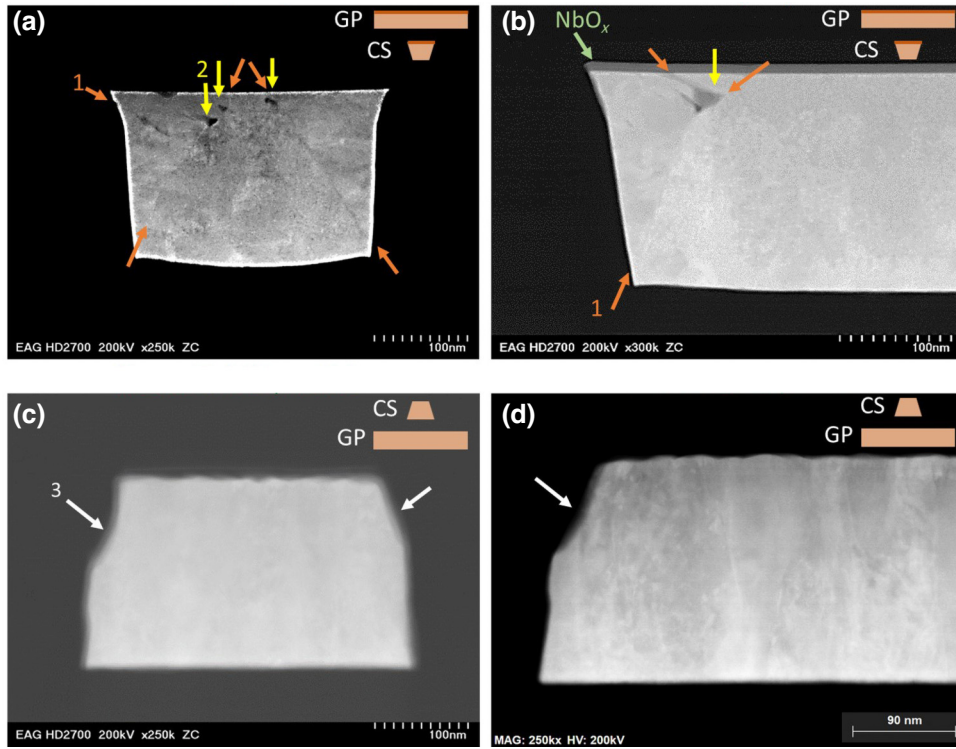


FIG. 7. STEM cross sections of the conducting strip for representative (a) 0.25- $\mu\text{m}$ - and (b) 1- $\mu\text{m}$ -wide MTL resonators from process A and (c) 0.25- $\mu\text{m}$ - and (d) 1- $\mu\text{m}$ -wide MTL resonators from process C. The sketches depict the corresponding MTL geometry. The image contrast in (a), (b), and (d) has been enhanced to highlight features, making NbO<sub>x</sub> invisible in (a). The orange arrows in (a) and (b) indicate the grain phase boundary between two Nb growth directions due to a damascene process. The yellow arrows in (a) and (b) indicate voids and/or vacancies in Nb. The white arrows in (c) and (d) indicate the “undercut” of the Nb during RIE.

times difference in the NbO thickness. Our results compare to those of Pambianchi *et al.*, who have observed a sevenfold increase in the surface resistance while there was no increase in the penetration depth of an N/S bilayer formed by 10-nm-thick Al sputtered onto 1- $\mu\text{m}$ -thick Nb versus bare Nb film, at 4.2 K and 11 GHz [118]. Thus, Fig. 4 is consistent with the NbO<sub>x</sub> layer comprising both insulating Nb<sub>2</sub>O<sub>5</sub> and metallic NbO: mostly NbO for process A and mostly Nb<sub>2</sub>O<sub>5</sub> for process B.

To interpret the surprising  $R_s < R_{\text{BCS}}$  for process C, assume that the Nb has a very thin NbO layer of thickness  $t^C$  due to O diffusion from SiO<sub>2</sub>, justified by Fig. 5(d). It is then intuitively clear that  $0 \lesssim t^C < t^B < t^A \lesssim 10$  nm, where  $t^B$  and  $t^A$  are the NbO thicknesses for the process-B ground plane and the process-A conducting strip, determined above. Assuming that  $t^C \sim 0.5$  nm and using  $13 \mu\Omega$ ,  $18 \mu\Omega$  and  $38 \mu\Omega$  for the respective bilayer surface resistances of processes C, B, and A, Fig. 6 shows  $R_{bl}$  normalized by  $R_{\text{BCS}} = 17 \mu\Omega$  as a function of  $t$ . The nonmonotonic dependence supports the Gurevich-Kubo theory that the pair-breaking mechanisms at the surface can bring  $R_{bl} < R_{\text{BCS}}$  [95,115]. This is associated with the N-layer effects broadening the gap peaks of ideal quasiparticle DOS [97], to remove a  $\sigma_1(\omega)$  divergence at  $\omega = 0$ , which is consistent with the  $R_s$  quadratic frequency

dependence of Fig. 2(c). Depending on the N/S regions contact resistance and the N-layer normal conductivity, a minimum of  $R_{bl}(t)$  is expected for  $t \sim 1$  nm, where the N-layer contribution increasing  $R_{bl}$  is small compared to the S-host contribution decreasing  $R_{bl}$  [119]. Our result also corroborates Oseroff *et al.*, who have decreased the surface resistance of bulk Nb by replacing the native oxide with a 0.1-nm-thick gold (Au) film, at 1.6–4.2 K and 4 and 5.2 GHz [120].

### B. $R_{s0}$ upturn at 0.25- $\mu\text{m}$ width

Another data trend seen in Fig. 4(a) is the 20–30% increase in  $R_{s0}$  for processes A and B at 0.25- $\mu\text{m}$  MTL width. The STEM cross sections in Figs. 7(a) and 7(b) show that the damascene process entails two Nb growth directions in the conducting strip: vertical growth from the trench bottom and horizontal growth from the trench sidewalls [121]. The two grain phases, a bottom grain and a sidewall grain, meet at an about 60° angle from the wafer plane. There are two such grain phase boundaries in both processes A and B, indicated by orange arrows in Figs. 7(a) and 7(b). Although EDS elemental analysis shows no Nb contamination at the boundaries, they possess voids and vacancies, indicated by yellow arrows.

Conversely, Figs. 7(c) and 7(d) confirm that the Cloisonné process C has only a vertically grown grain.

Aligned with the rf current flow, the grain phase boundaries may not affect its distribution in the straight segments of the conducting strip while can impede at the right-angle bends. Besides, the sidewall grain morphology along with the voids and vacancies can reduce the electron mean free path  $l_{mfp}$ . Since  $R_{BCS} \propto l_{mfp} (1 + \xi_0/l_{mfp})^{3/2}$  has a minimum at  $l_{mfp} = \xi_0/2$ , where  $\xi_0 \sim 33\text{--}39$  nm is the Nb microscopic coherence length [37,95], reducing  $l_{mfp}$  below that increases  $R_s$ . Voids can also provide Nb hydride formation sites [122,123], where H diffusion creates normal-conducting precipitates. Subject to the proximity effect, hydrides suppress superconductivity in a host Nb.

Decreasing the conducting-strip width  $w$  increases the sidewall grain and void fractions, the geometry of which is determined by the trench depth  $d$ . For instance, the grain fraction increases from 20% in a 1- $\mu\text{m}$ -wide strip up to 50% in a 0.25- $\mu\text{m}$ -wide strip. Since for a 0.25- $\mu\text{m}$ -wide MTL the conducting strip dominates the averaged resistance, its upturn in Fig. 4(a) can be attributed to the damascene effects.

## VI. CONCLUSIONS AND OUTLOOK

We have successfully disentangled and quantified comparable superconductor and dielectric microwave losses by exploiting their frequency dependence in a multi-mode microstrip resonator. The adoption of HFSS to solve a superconductor interior overcomes a limitation of the SIBC-based modeling to interconnects much bigger than  $\lambda$ . From the HFSS solution, we obtain the resonator geometric factor, which allows us to extract  $R_s$  and  $\tan \delta$  with only a single simulation per MTL geometry. The method is representative of SCE interconnects and applies to any transmission line including a strip line and a coplanar waveguide, as well as a via chain, to analyze the via loss. The technology is suitable for optimization and statistical process control of both digital and quantum SCE fabrication.

Using the method, we have optimized a 0.25- $\mu\text{m}$  Nb/SiO<sub>2</sub> planarized process for minimum interconnect loss in the gigahertz range. The superconductor intrinsic resistance  $R_s$  and dielectric loss tangent  $\tan \delta$  have been directly compared between different processing conditions, stack geometries, and line widths. Correlating  $R_s$  with the STEM and EDS analysis has revealed the extraneous loss mechanisms for damascene processing, including the Nb plasma oxidation and grain-growth orientation. A difference in  $R_s$  between the two damascene processes is explained by the difference in the NbO thickness. This has led us to a Cloisonné process, free of the above effects, demonstrating  $R_s = 13 \pm 1.4 \mu\Omega$  down to 0.25- $\mu\text{m}$  line width, which is even lower than the Nb minimum BCS resistance  $R_{BCS} \approx 17 \mu\Omega$  at 4.2 K and 10 GHz [96,112]. This corroborates the

Gurevich-Kubo theory that a very thin metallic overlayer (NbO in our case) can reduce the superconductor  $R_s$  below  $R_{BCS}$  [115]. Thus, contrary to our initial expectations, neither CMP nor RIE nor SiO<sub>2</sub> poisoning may increase the Nb resistive loss. With  $\tan \delta = 0.0012 \pm 0.0001$  independent of processing conditions and MTL geometry, the TEOS-derived SiO<sub>2</sub> is a very attractive insulator for highly integrated SCE, the fairly high dielectric loss of which can be attributed to a low-temperature PECVD.

With the Nb wires already at or below the theoretical minimum loss, future SCE interconnect optimization calls for lower loss materials. For instance, a dielectric with  $\tan \delta = 10^{-4}$  would improve the energy efficiency of an RQL resonant clock network [14] from 30% to 80–90%. Since SiO<sub>2</sub> does not poison Nb, increasing the deposition temperature may reduce the  $\tan \delta$ , without affecting Nb. Furthermore, the use of a very thin metallic overlayer could reduce the Nb  $R_s$  [98,120]. Conversely, higher- $T_c$  superconductors such as NbTiN can be explored [7]. Depending on the ratio of the conductor and dielectric geometric factors, optimizing one material could be more beneficial than another.

Our loss-data deconvolution method relies on conjectured frequency dependencies for  $R_s$  and  $\tan \delta$ . Using a longer resonator to increase the spectrum and the mode density, while allowing  $a$  and  $p$  as fitting parameters in Eq. (6), one may unambiguously determine frequency-scaling exponents for  $R_s$  and  $\tan \delta$ , to gain new insights into their mechanisms.

## ACKNOWLEDGMENTS

We acknowledge Pavel Borodulin and Edward Kurek for the test-fixture design, Jay Walters, Andrew Brownfield and David Vermillion for coordinating the design and test, Justin Goodman and Dr. Steve Sendelbach for assisting with data analysis, Dr. Eric Jones for assistance with the STEM and EDS analysis, Dr. Henry Luo for the SQUID penetration-depth measurements, and Dr. Flavio Griggio and Professor Dr. Alex Gurevich for fruitful discussions. V.V.T. acknowledges stimulating discussions with David Gill. All STEM and EDS characterizations were done at EAG Laboratories [124]. S.M.A. acknowledges support from the National Science Foundation through Grant No. NSF DMR-2004386, and the U.S. Department of Energy–High Energy Physics through Grant No. #DESC0017931. This research is based on work supported in part by the Office of the Director of National Intelligence (ODNI) and the Intelligence Advanced Research Projects Activity (IARPA), via the U.S. Army Research Office (ARO), Contract No. W911NF-14-C-0116. The views and conclusions contained herein are those of the authors and should not be interpreted as necessarily representing the official policies or endorsements, either expressed

or implied, of the NSF, the U.S. Department of Energy (DOE), the ODNI, the IARPA, or the U.S. Government.

### APPENDIX A: GEOMETRIC FACTOR OF TRANSMISSION-LINE RESONATOR

The telegrapher's RLGC parameters of a superconducting transmission line are as follows [52,82,125]:

$$R = \frac{2}{|I|^2} \int_A R_s \lambda |\mathbf{J}|^2 da \approx \frac{2R_{\text{eff}}}{w}, \quad (\text{A1a})$$

$$L = \frac{\mu_0}{|I|^2} \int_A (|\mathbf{H}|^2 + \lambda^2 |\mathbf{J}|^2) da \approx \mu_0 \frac{s + 2\lambda_{\text{eff}}}{w}, \quad (\text{A1b})$$

$$G = \frac{\omega \varepsilon_0}{|V|^2} \int_A \tan \delta \varepsilon_r |\mathbf{E}|^2 da \approx \omega \varepsilon_0 \varepsilon_r \tan \delta \frac{w}{s}, \quad (\text{A1c})$$

$$C = \frac{\varepsilon_0}{|V|^2} \int_A \varepsilon_r |\mathbf{E}|^2 da \approx \varepsilon_0 \varepsilon_r \frac{w}{s}, \quad (\text{A1d})$$

where  $R$ ,  $L$ ,  $G$ , and  $C$  are the respective resistance, inductance, conductance, and capacitance per unit length of the line,  $\varepsilon_0$  and  $\mu_0$  are the vacuum permittivity and permeability,  $\omega$  is the angular frequency,  $I$  and  $V$  are the current and voltage, the integrals are over the line cross section  $A$ ,  $R_s$  and  $\lambda$  are the intrinsic microwave resistance and penetration depth,  $\varepsilon_r$  and  $\tan \delta$  are the relative dielectric constant and the loss tangent,  $\mathbf{J}$ ,  $\mathbf{H}$ , and  $\mathbf{E}$  are the vector current density, magnetic field, and electric field, and  $\sigma_1 \ll \sigma_2$  is assumed in Eqs. (A1a) and (A1b). The first addend in the integrand of Eq. (A1b) is due to the magnetic energy stored both outside and inside the superconducting wires, while the second addend is due to the kinetic energy stored in the superconducting carriers [82]. To provide a simple analytical reference, the approximations on the right of Eqs. (A1) pertain a parallel-plate line (wide microstrip) formed by a dielectric spacer of thickness  $s$  sandwiched between two superconducting plates of thickness  $d$  and width  $w \gg s$  [42]. The effective surface resistance  $R_{\text{eff}} = R_s [\coth(d/\lambda) + (d/\lambda)/\sinh^2(d/\lambda)]$  and the effective penetration depth  $\lambda_{\text{eff}} = \lambda \coth(d/\lambda)$  address the finite plate thickness [79], where the transmission loss is ignored.

The internal  $Q$  factor of a transmission-line resonator can be expressed as [52]

$$\frac{1}{Q_i} = \frac{R}{\omega L} + \frac{G}{\omega C}, \quad (\text{A2})$$

where the first and second addends represent the conductor and dielectric loss, respectively, and the radiation loss is ignored. For a resonator comprising  $M$  conductors and  $N$  dielectric layers or tubes, substituting Eqs. (A1) into

Eq. (A2) gives

$$\frac{1}{Q_i} = \sum_{m=1}^M \frac{\langle R_{sm} \rangle}{\Gamma_{cm}} + \sum_{n=1}^N \frac{\langle \tan \delta_n \rangle}{\Gamma_{dn}}. \quad (\text{A3})$$

Here, the global partial intrinsic resistance of the  $m$ th conductor and the dielectric loss tangent of the  $n$ th dielectric are

$$\langle R_{sm} \rangle = \frac{\int_{A_m} R_s \lambda |\mathbf{J}|^2 da}{\int_{A_m} \lambda |\mathbf{J}|^2 da}, \quad (\text{A4a})$$

$$\langle \tan \delta_n \rangle = \frac{\int_{A_n} \tan \delta \varepsilon_r |\mathbf{E}|^2 da}{\int_{A_n} \varepsilon_r |\mathbf{E}|^2 da}, \quad (\text{A4b})$$

where  $A_m$  and  $A_n$  are the respective cross sections of the  $m$ th conductor and the  $n$ th dielectric. For the spatially homogeneous loss,  $\langle R_{sm} \rangle = R_{sm}$  and  $\langle \tan \delta_n \rangle = \tan \delta_n$ , while  $\lambda$  and  $\varepsilon_r$  can be inhomogeneous. Furthermore, in Eq. (A3), the partial geometric factors associated with respective loss in the  $m$ th conductor and  $n$ th dielectric are

$$\Gamma_{cm} = \omega \mu_0 \frac{\int_A (|\mathbf{H}|^2 + \lambda^2 |\mathbf{J}|^2) da}{2 \int_{A_m} \lambda |\mathbf{J}|^2 da}, \quad (\text{A5a})$$

$$\Gamma_{dn} = \frac{\int_A \varepsilon_r |\mathbf{E}|^2 da}{\int_{A_n} \varepsilon_r |\mathbf{E}|^2 da}. \quad (\text{A5b})$$

The conductor geometric factor  $\Gamma_c$  has units of ohms and is exclusively determined by the line cross-section geometry and  $\lambda$ . A good superconductor with  $\sigma_1 \ll \sigma_2$  has dispersionless  $\lambda$ , making  $\Gamma_c \propto \omega$ . The dielectric geometric factor  $\Gamma_d$  is unitless and is exclusively determined by the line cross-section geometry and  $\varepsilon_r$ . For the dispersionless  $\varepsilon_r$ ,  $\Gamma_d$  is frequency independent. Setting  $M = 2$  and  $N = 3$  in Eq. (A3) leads to Eqs. (3), (8), and (9).

For reference, let us compare the geometric factors of the transmission-line resonator to those of voluminous resonators. Equation (A5a) is analogous to a cavity partial geometric factor [35,38,126],

$$G_m = \omega \mu_0 \frac{\int_V |\mathbf{H}|^2 dv}{\int_{S_m} |\mathbf{H}_\tau|^2 ds}, \quad (\text{A6})$$

where the integrals are over the cavity volume  $V$  and the  $m$ th wall surface  $S_m$ , the fields are taken from a perfect-conductor cavity of the same geometry, and  $\mathbf{H}_\tau$  is the tangential magnetic field at the wall. Giving a cavity inverse  $Q$  factor  $Q_{\text{cav}}^{-1} = \sum_{m=1}^M \text{Re}(Z_s)/G_m$ , the definition in Eq. (A6) uses a perturbation approach involving the Leontovich boundary condition (SIBC)  $\mathbf{E}_\tau = Z_s \mathbf{H}_\tau \times \mathbf{n}$ , where  $\mathbf{E}_\tau$  is the tangential electric field at the impedance surface,  $Z_s$  is the intrinsic impedance, and  $\mathbf{n}$  is the inward unit vector normal to the surface [75–78]. Likewise,

$Q_{\text{cav}} = \omega\mu_0 D/R_s$ , where  $D$  is the characteristic length scale about the smallest dimension of a cavity [126]. For instance,  $D = s/2$  for a parallel-plate resonator [39]. Thus, assuming that the wall-curvature radius is much greater than  $\lambda$ , Eq. (A6) is inapplicable to submicron MTL with  $w \sim d \sim \lambda$ . Besides, neglecting the magnetic and kinetic energies stored inside a superconductor, Eq. (A6) requires  $D \gg \lambda$ , which conflicts with  $D \sim s \sim \lambda$ . Equation (A5b) is analogous to the inverse of a dielectric resonator (DR) electric energy-filling factor [45],

$$\frac{1}{p_n} = \frac{\int_V \varepsilon_r |\mathbf{E}|^2 dv}{\int_{V_n} \varepsilon_r |\mathbf{E}|^2 dv}, \quad (\text{A7})$$

where the integrals are over the resonator volume  $V$  and the  $n$ th dielectric member volume  $V_n$  and  $\varepsilon_r$  is the spatially dependent dielectric constant. The inverse  $Q$  factor of DR is  $Q_{DR}^{-1} = \sum_{n=1}^N p_n \tan \delta_n$ . A compound resonator thus has  $Q_i^{-1} = Q_{\text{cav}}^{-1} + Q_{DR}^{-1}$ , analogous to Eq. (A3).

## APPENDIX B: $Q$ FACTOR OF PARALLEL-PLATE RESONATOR

Substitution of the approximations from Eqs. (A1) into Eq. (A2) gives the partial  $Q$  factors of a parallel-plate transmission-line resonator [42]:

$$Q_{cPP} = \frac{\omega\mu_0 [s + 2\lambda \coth(d/\lambda)]}{2R_s [\coth(d/\lambda) + (d/\lambda)/\sinh^2(d/\lambda)]}, \quad (\text{B1a})$$

$$Q_{dPP} = 1/\tan \delta, \quad (\text{B1b})$$

where the first addend in the denominator brackets of Eq. (B1a) accounts for the magnetic energy stored between the plates (external geometric inductance) and the second addend accounts for both the magnetic energy stored in the magnetic field penetrating the plate (internal geometric inductance) and the kinetic energy stored in the superconducting carriers (kinetic inductance) [127]. The internally stored energies are equal in the thick-plate case  $d \gg \lambda$ , whereas the kinetic energy dominates the thin plate  $d < \lambda$  [128]. The supercurrent kinetic energy dominates the inductive energy in our MTL resonators, due to  $s < 2\lambda_{\text{eff}}$ . Multiplying both sides of Eq. (B1a) by  $R_s$  leads to Eq. (11a). Equation (B1b) leads to Eq. (11b).

In the limit  $s \gg 2\lambda_{\text{eff}}$ , Eq. (B1a) reduces to  $\omega\mu_0 s/2R_{\text{eff}}$ , following from Eq. (A6). In the limit  $s \ll 2\lambda_{\text{eff}}$ , Eq. (B1a) gives the surface-impedance quality factor  $\omega\mu_0 \lambda_{\text{eff}}/R_{\text{eff}} \propto X_s/R_s$  [129]. Decreasing  $s$  to few nanometers transforms the electromagnetic oscillations into the Josephson plasma oscillations [130]. Applying Eq. (A7) to the parallel-plate resonator also gives Eq. (B1b).

## APPENDIX C: DERIVATION OF EQS. (12)

Consider a two-port network formed by a transmission line of length  $l$ . The  $ABCD$  (transmission) matrix of such a

network is [131]

$$\begin{bmatrix} A & B \\ C & D \end{bmatrix} = \begin{bmatrix} \cosh(\gamma l) & Z_{TL} \sinh(\gamma l) \\ Z_{TL}^{-1} \sinh(\gamma l) & \cosh(\gamma l) \end{bmatrix}, \quad (\text{C1})$$

where  $\gamma$  is the propagation constant, and  $Z_{TL}$  is the characteristic impedance. For the electrically short network, a quadratic Taylor expansion about  $\gamma l = 0$  gives  $\cosh(\gamma l) \approx 1 + (\gamma l)^2/2$  and  $\sinh(\gamma l) \approx \gamma l$ . A general transmission line has  $\gamma = \sqrt{ZY}$  and  $Z_{TL} = \sqrt{Z/Y}$ , where  $Z$  and  $Y$  are the series impedance and shunt admittance per unit length [111]. Substituting those into Eq. (C1) gives

$$\begin{bmatrix} A & B \\ C & D \end{bmatrix} \approx \begin{bmatrix} 1 + \frac{1}{2}ZYl^2 & Zl \\ \frac{1}{Yl} & 1 + \frac{1}{2}ZYl^2 \end{bmatrix}. \quad (\text{C2})$$

By reciprocity, the elements of the  $Z$ -parameter matrix [52] corresponding to the  $ABCD$  matrix of Eq. (C2) are  $Z_{11} = Z_{22} = (Yl)^{-1} + Zl/2$  and  $Z_{12} = Z_{21} = (Yl)^{-1}$ . Solving these equations for  $Z$  and  $Y$  leads to Eqs. (12).

## APPENDIX D: SURFACE IMPEDANCE OF N/S BILAYER

Consider an N/S bilayer formed by an N layer of thickness  $t$  on top of an S host. Assume that the N layer is subject to local electrodynamics and that there is no proximity coupling between the N and S regions. Then, an impedance-transformation method [52] gives the bilayer surface impedance,

$$Z_{bl} = R_{bl} + iX_{bl} = Z_n \frac{Z_h + Z_n \tanh(\gamma_n t)}{Z_n + Z_h \tanh(\gamma_n t)}. \quad (\text{D1})$$

Here,  $R_{bl}$  and  $X_{bl} = \omega\mu_0 \lambda_{bl}$  are the bilayer surface resistance and reactance, in which  $\lambda_{bl}$  is the global penetration depth,  $Z_n = \omega\mu_0 \delta_{sk}(1+i)/2$  and  $\gamma_n = (1+i)/\delta_{sk}$  are the metal wave impedance and propagation constant,  $\delta_{sk} = \sqrt{2/\omega\mu_0 \sigma_n}$  is the metal skin depth, in which  $\sigma_n$  being the bulk conductivity, and  $Z_h = R_h + i\omega\mu_0 \lambda_h$  is the S-host surface impedance, in which  $R_h$  and  $\lambda_h$  are the surface resistance and the penetration depth, respectively. Using  $\tanh(\gamma_n t) \approx \gamma_n t$  for  $t \ll \delta_{sk}$ , separating the real and imaginary parts, and dropping small terms due to  $t \ll \delta_{sk}$  and  $R_h \ll \omega\mu_0 \delta_{sk} \sim \omega\mu_0 \lambda_h$ , Eq. (D1) leads to the bilayer surface resistance and reactance

$$R_{bl} = \omega^2 \mu_0^2 \lambda_h (\lambda_h + t) t \sigma_n + R_h, \quad (\text{D2a})$$

$$X_{bl} = \omega\mu_0 (\lambda_h + t). \quad (\text{D2b})$$

[1] K. Likharev, O. Mukhanov, and V. Semenov, in *SQUID '85 Superconducting Quantum Interference*



- Devices and their Applications* (De Gruyter, Berlin (West), Germany, 1986), p. 1103.
- [2] K. K. Likharev and V. K. Semenov, RSFQ logic/memory family: A new Josephson-junction technology for subterahertz-clock-frequency digital systems, *IEEE Trans. Appl. Supercond.* **1**, 3 (1991).
  - [3] H. Hayakawa, N. Yoshikawa, S. Yorozu, and A. Fujimaki, Superconducting digital electronics, *Proc. IEEE* **92**, 1549 (2004).
  - [4] R. Peterson and D. McDonald, Picosecond pulses from Josephson junctions: Phenomenological and microscopic analyses, *IEEE Trans. Magn.* **13**, 887 (1977).
  - [5] Y. Yamanashi, T. Kainuma, N. Yoshikawa, I. Kataeva, H. Akaike, A. Fijumaki, M. Tnaka, N. Takagi, S. Nagasawa, and M. Hidaka, 100 GHz demonstrations based on the single-flux-quantum cell library for the 10 kA/cm<sup>2</sup> Nb multi-layer process, *IEICE Trans. Electron.* **E93-C**, 440 (2010).
  - [6] S. K. Tolpygo, Superconductor digital electronics: Scalability and energy efficiency issues (review article), *Low Temp. Phys.* **42**, 361 (2016).
  - [7] A. Herr, Q. Herr, S. Brebels, M.-S. Kim, A. Pokhrel, B. Hodges, T. Josephsen, S. ONeal, R. Bai, K. Nowack, A.-M. Valente-Feliciano, and Z. Tökei, Scaling NbTiN-based ac-powered Josephson digital to 400M devices/cm<sup>2</sup>, [arXiv:2303.16792](https://arxiv.org/abs/2303.16792) (2023).
  - [8] M. Hosoya, W. Hioe, J. Casas, R. Kamikawai, Y. Harada, Y. Wada, H. Nakane, R. Suda, and E. Goto, Quantum flux parametron: A single quantum flux device for Josephson supercomputer, *IEEE Trans. Appl. Supercond.* **1**, 77 (1991).
  - [9] Q. P. Herr, A. Y. Herr, O. T. Oberg, and A. G. Ioannidis, Ultra-low-power superconductor logic, *J. Appl. Phys.* **109**, 103903 (2011).
  - [10] M. H. Volkmann, A. Sahu, C. J. Fourie, and O. A. Mukhanov, Implementation of energy efficient single flux quantum digital circuits with sub-aJ/bit operation, *Supercond. Sci. Technol.* **26**, 015002 (2012).
  - [11] N. Takeuchi, D. Ozawa, Y. Yamanashi, and N. Yoshikawa, An adiabatic quantum flux parametron as an ultra-low-power logic device, *Supercond. Sci. Technol.* **26**, 035010 (2013).
  - [12] N. Magen, A. Kolodny, U. Weiser, and N. Shamir, in *Proceedings of the 2004 International Workshop on System Level Interconnect Prediction* (ACM, Paris, France, 2004).
  - [13] L. Chang, D. J. Frank, R. K. Montoye, S. J. Koester, B. L. Ji, P. W. Coteus, R. H. Dennard, and W. Haensch, Practical strategies for power-efficient computing technologies, *Proc. IEEE* **98**, 215 (2010).
  - [14] J. A. Strong, V. V. Talanov, M. E. Nielsen, A. C. Brownfield, N. Bailey, Q. P. Herr, and A. Y. Herr, A resonant metamaterial clock distribution network for superconducting logic, *Nat. Electron.* **5**, 171 (2022).
  - [15] IRDS, International roadmap for devices and systems: Cryogenic electronics and quantum information processing, <https://irds.ieee.org/editions/2022> (2022).
  - [16] Y. W. Kim, Y. H. Kahng, J.-H. Choi, and S.-G. Lee, Critical properties of submicrometer-patterned Nb thin film, *IEEE Trans. Appl. Supercond.* **19**, 2649 (2009).
  - [17] S. K. Tolpygo, E. B. Golden, T. J. Weir, and V. Bolkhovsky, Inductance of superconductor integrated circuit features with sizes down to 120 nm, *Supercond. Sci. Technol.* **34**, 085005 (2021).
  - [18] A. Ramzi, S. A. Charlebois, and P. Krantz, Niobium and aluminum Josephson junctions fabricated with a damascene CMP process, *Phys. Procedia* **36**, 211 (2012).
  - [19] S. Nagasawa, T. Satoh, K. Hinode, Y. Kitagawa, M. Hidaka, H. Akaike, A. Fujimaki, K. Takagi, N. Takagi, and N. Yoshikawa, New Nb multi-layer fabrication process for large-scale SFQ circuits, *Phys. C: Supercond.* **469**, 1578 (2009).
  - [20] C. Kaanta, W. Cote, J. Cronin, K. Holland, P.-I. Lee, and T. Wright, in *1987 International Electron Devices Meeting* (IEEE, 1987), p. 209.
  - [21] W. L. Guthrie, W. J. Patrick, E. Levine, H. C. Jones, E. A. Mehter, T. F. Houghton, G. T. Chiu, and M. A. Fury, A four-level VLSI bipolar metallization design with chemical-mechanical planarization, *IBM J. Res. Dev.* **36**, 845 (1992).
  - [22] M. Krishnan, J. W. Nalaskowski, and L. M. Cook, Chemical mechanical planarization: Slurry chemistry, materials, and mechanisms, *Chem. Rev.* **110**, 178 (2010).
  - [23] M. Grundner and J. Halbritter, XPS and AES studies on oxide growth and oxide coatings on niobium, *J. Appl. Phys.* **51**, 397 (1980).
  - [24] S. K. Tolpygo, D. Amparo, R. T. Hunt, J. A. Vivalda, and D. T. Yohannes, Diffusion stop-layers for superconducting integrated circuits and qubits with Nb-based Josephson junctions, *IEEE Trans. Appl. Supercond.* **21**, 119 (2011).
  - [25] D. Grieg and H. Engelmann, Microstrip—a new transmission technique for the kilomegacycle range, *Proc. IRE* **40**, 1644 (1952).
  - [26] J. Egan, M. Nielsen, J. Strong, V. Talanov, E. Rudman, B. Song, Q. Herr, and A. Herr, Synchronous chip-to-chip communication with a multi-chip resonator clock distribution network, *Supercond. Sci. Technol.* **35**, 105010 (2022).
  - [27] H. Dai, C. Kegerreis, D. W. Gamage, J. Egan, M. Nielsen, Y. Chen, D. Tuckerman, S. Peek, B. Yelamanchili, M. Hamilton, *et al.*, Isochronous data link across a superconducting Nb flex cable with 5 femtojoules per bit, *Supercond. Sci. Technol.* **35**, 045014 (2022).
  - [28] R. L. Kautz, Picosecond pulses on superconducting striplines, *J. Appl. Phys.* **49**, 308 (1978).
  - [29] V. V. Talanov, D. Knee, D. Harms, K. Perkins, A. Urbanas, J. Egan, Q. Herr, and A. Herr, Propagation of picosecond pulses on superconducting transmission line interconnects, *Supercond. Sci. Technol.* **35**, 055011 (2022).
  - [30] J. Volk, A. Wynn, E. Golden, T. Sherwood, and G. Tzimpragos, Addressable superconductor integrated circuit memory from delay lines, *Sci. Rep.* **13** (2023).
  - [31] A. B. Pippard, The surface impedance of superconductors and normal metals at high frequencies I. Resistance of superconducting tin and mercury at 1200 Mcyc./sec, *Proc. R. Soc. Lond. A. Math. Phys. Sci.* **191**, 370 (1947).
  - [32] W. M. Fairbank, High frequency surface resistivity of tin in the normal and superconducting states, *Phys. Rev.* **76**, 1106 (1949).

- [33] E. Maxwell, P. Marcus, and J. C. Slater, Surface impedance of normal and superconductors at 24,000 megacycles per second, *Phys. Rev.* **76**, 1332 (1949).
- [34] V. Braginsky, V. Mitrofanov, V. Panov, and R. Krotkov, *Systems with Small Dissipation* (University of Chicago Press, Chicago, IL, USA, 1987). <https://press.uchicago.edu/ucp/books/book/chicago/S/bo5973099.html>.
- [35] J. Turneaure, J. Halbritter, and H. Schwettman, The surface impedance of superconductors and normal conductors: The Mattis-Bardeen theory, *J. Supercond.* **4**, 341 (1991).
- [36] N. Newman and W. G. Lyons, High-temperature superconducting microwave devices: Fundamental issues in materials, physics, and engineering, *J. Supercond.* **6**, 119 (1993).
- [37] C. Benvenuti, S. Calatroni, I. Campisi, P. Darriulat, M. Peck, R. Russo, and A.-M. Valente, Study of the surface resistance of superconducting niobium films at 1.5 GHz, *Phys. C: Supercond.* **316**, 153 (1999).
- [38] M. Hein, *High-Temperature-Superconductor Thin Films at Microwave Frequencies* (Springer Science & Business Media, Berlin, Germany, 1999), Vol. 155.
- [39] R. Taber, A parallel plate resonator technique for microwave loss measurements on superconductors, *Rev. Sci. Instrum.* **61**, 2200 (1990).
- [40] J. S. Martens, V. M. Hietala, D. S. Ginley, T. E. Zipperian, and G. K. G. Hohenwarter, Confocal resonators for measuring the surface resistance of high-temperature superconducting films, *Appl. Phys. Lett.* **58**, 2543 (1991).
- [41] J. Mazierska, Dielectric resonator as a possible standard for characterization of high temperature superconducting films for microwave applications, *J. Supercond.* **10**, 73 (1997).
- [42] V. V. Talanov, L. V. Mercaldo, S. M. Anlage, and J. H. Claassen, Measurement of the absolute penetration depth and surface resistance of superconductors and normal metals with the variable spacing parallel plate resonator, *Rev. Sci. Instrum.* **71**, 2136 (2000).
- [43] S. M. Anlage, Microwave superconductivity, *IEEE J. Microw.* **1**, 389 (2021).
- [44] C. Zuccaro, M. Winter, N. Klein, and K. Urban, Microwave absorption in single crystals of lanthanum aluminate, *J. Appl. Phys.* **82**, 5695 (1997).
- [45] J. Krupka, K. Derzakowski, B. Riddle, and J. Baker-Jarvis, A dielectric resonator for measurements of complex permittivity of low loss dielectric materials as a function of temperature, *Meas. Sci. Technol.* **9**, 1751 (1998).
- [46] C. Kaiser, *High Quality Nb/Al-AlO<sub>x</sub>/Nb Josephson Junctions: Technological Development and Macroscopic Quantum Experiments* (KIT Scientific Publishing, Karlsruhe, Germany, 2011), Vol. 4.
- [47] D. B. Tuckerman, M. C. Hamilton, D. J. Reilly, R. Bai, G. A. Hernandez, J. M. Hornibrook, J. A. Sellers, and C. D. Ellis, Flexible superconducting Nb transmission lines on thin film polyimide for quantum computing applications, *Supercond. Sci. Technol.* **29**, 084007 (2016).
- [48] C. R. H. McRae, H. Wang, J. Gao, M. R. Vissers, T. Brecht, A. Dunsworth, D. P. Pappas, and J. Mutus, Materials loss measurements using superconducting microwave resonators, *Rev. Sci. Instrum.* **91**, 091101 (2020).
- [49] P. V. Mason and R. W. Gould, Slow-wave structures utilizing superconducting thin-film transmission lines, *J. Appl. Phys.* **40**, 2039 (1969).
- [50] S. M. Anlage, H. Sze, H. J. Snortland, S. Tahara, B. Langley, C.-B. Eom, M. Beasley, and R. Taber, Measurements of the magnetic penetration depth in YBa<sub>2</sub>Cu<sub>3</sub>O<sub>7- $\delta$</sub>  thin films by the microstrip resonator technique, *Appl. Phys. Lett.* **54**, 2710 (1989).
- [51] B. W. Langley, S. M. Anlage, R. F. W. Pease, and M. R. Beasley, Magnetic penetration depth measurements of superconducting thin-films by a microstrip resonator technique, *Rev. Sci. Instrum.* **62**, 1801 (1991).
- [52] D. M. Pozar, *Microwave Engineering* (John Wiley & Sons, Hoboken, NJ, USA, 2011), 4th ed.
- [53] J. Halbritter, On the oxidation and on the superconductivity of niobium, *Appl. Phys. A Solids Surf.* **43**, 1 (1987).
- [54] C. Wang, C. Axline, Y. Y. Gao, T. Brecht, Y. Chu, L. Frunzio, M. H. Devoret, and R. J. Schoelkopf, Surface participation and dielectric loss in superconducting qubits, *Appl. Phys. Lett.* **107**, 162601 (2015).
- [55] W. Woods, G. Calusine, A. Melville, A. Sevi, E. Golden, D. Kim, D. Rosenberg, J. Yoder, and W. Oliver, Determining interface dielectric losses in superconducting coplanar-waveguide resonators, *Phys. Rev. Appl.* **12**, 014012 (2019).
- [56] A. Melville, G. Calusine, W. Woods, K. Serniak, E. Golden, B. M. Niedzielski, D. K. Kim, A. Sevi, J. L. Yoder, E. A. Dauler, and W. D. Oliver, Comparison of dielectric loss in titanium nitride and aluminum superconducting resonators, *Appl. Phys. Lett.* **117**, 124004 (2020).
- [57] A. Megrant, C. Neill, R. Barends, B. Chiaro, Y. Chen, L. Feigl, J. Kelly, E. Lucero, M. Mariantoni, P. J. O'Malley, *et al.*, Planar superconducting resonators with internal quality factors above one million, *Appl. Phys. Lett.* **100**, 113510 (2012).
- [58] M. S. Khalil, M. Stoutimore, F. Wellstood, and K. Osborn, An analysis method for asymmetric resonator transmission applied to superconducting devices, *J. Appl. Phys.* **111**, 054510 (2012).
- [59] P. G. Baity, C. Maclean, V. Seferai, J. Bronstein, Y. Shu, T. Hemakumara, and M. Weides, Circle fit optimization for resonator quality factor measurements: Point redistribution for maximal accuracy, [arXiv:2301.06364](https://arxiv.org/abs/2301.06364) (2023).
- [60] E. Belohoubek and E. Denlinger, Loss considerations for microstrip resonators (short papers), *IEEE. Trans. Microw. Theory Tech.* **23**, 522 (1975).
- [61] N. Cherpak, A. Barannik, Y. Filipov, Y. Prokopenko, and S. Vitusevich, Accurate microwave technique of surface resistance measurement of large-area HTS films using sapphire quasi-optical resonator, *IEEE Trans. Appl. Supercond.* **13**, 3570 (2003).
- [62] N. Klein, G. Müller, H. Piel, B. Roas, L. Schultz, U. Klein, and M. Peiniger, Millimeter wave surface resistance of epitaxially grown YBa<sub>2</sub>Cu<sub>3</sub>O<sub>7- $x$</sub>  thin films, *Appl. Phys. Lett.* **54**, 757 (1989).
- [63] C. Wilker, Z.-Y. Shen, V. Nguyen, and M. Brenner, in *41st ARFTG Conference Digest*, Vol. 23 (IEEE, 1993), p. 38.
- [64] J. Krupka, K. Derzakowski, M. Tobar, J. Hartnett, and R. G. Geyer, Complex permittivity of some ultralow loss

- dielectric crystals at cryogenic temperatures, *Meas. Sci. Technol.* **10**, 387 (1999).
- [65] J. Krupka, J. Breeze, A. Centeno, N. Alford, T. Claussen, and L. Jensen, Measurements of permittivity, dielectric loss tangent, and resistivity of float-zone silicon at microwave frequencies, *IEEE Trans. Microw. Theory Tech.* **54**, 3995 (2006).
- [66] K. Cicak, D. Li, J. A. Strong, M. S. Allman, F. Altomare, A. J. Sirois, J. D. Whittaker, J. D. Teufel, and R. W. Simmonds, Low-loss superconducting resonant circuits using vacuum-gap-based microwave components, *Appl. Phys. Lett.* **96**, 093502 (2010).
- [67] M. A. Golosovsky, H. J. Snortland, and M. R. Beasley, Nonlinear microwave properties of superconducting Nb microstrip resonators, *Phys. Rev. B* **51**, 6462 (1995).
- [68] D. E. Oates, S. K. Tolpygo, and V. Bolkhovskiy, Submicron Nb microwave transmission lines and components for single-flux-quantum and analog large-scale superconducting integrated circuits, *IEEE Trans. Appl. Supercond.* **27**, 1 (2017).
- [69] A. Y. Basovich, R. K. Belov, V. A. Markelov, L. A. Mazo, S. A. Pavlov, V. V. Talanov, and A. V. Varganov, Parallel-plate resonator of variable spacer thickness for accurate measurements of surface impedance of high- $T_c$  superconductive films, *J. Supercond.* **5**, 497 (1992).
- [70] G. Yassin and S. Withington, Electromagnetic models for superconducting millimetre-wave and sub-millimetre-wave microstrip transmission lines, *J. Phys. D: Appl. Phys.* **28**, 1983 (1995).
- [71] M. R. Rafique, I. Kataeva, H. Engseth, M. Tarasov, and A. Kidiyarova-Shevchenko, Optimization of superconducting microstrip interconnects for rapid single-flux-quantum circuits, *Supercond. Sci. Technol.* **18**, 1065 (2005).
- [72] V. Belitsky, C. Risacher, M. Pantaleev, and V. Vassilev, Superconducting microstrip line model studies at millimetre and sub-millimetre waves, *Int. J. Infrared Millimeter Waves* **27**, 809 (2006).
- [73] K. U-Yen, K. Rostem, and E. J. Wollack, Modeling strategies for superconducting microstrip transmission line structures, *IEEE Trans. Appl. Supercond.* **28**, 1 (2018).
- [74] M. H. Amini and A. Mallahzadeh, Modeling of superconducting components in full-wave simulators, *J. Supercond. Nov. Magn.* **34**, 675 (2021).
- [75] M. Leontovich, A new method to solve problems of EM wave propagation over the earth surface, *USSR Acad. Sci. Trans., Phys. Ser.* **8**, 16 (1944).
- [76] M. Leontovich, Approximate boundary conditions for the electromagnetic field on the surface of a good conductor, *Invest. Radiowave Propag.* **2**, 5 (1948).
- [77] M. A. Miller and V. I. Talanov, The use of the surface impedance concept in the theory of electromagnetic surface waves, in *Onde superficiali*, edited by G. T. di Francia (Springer-Verlag, Berlin, 2011), p. 257, [in Russian—*Izvestia VUZov Radiofizika* **4**, 795–830 (1961)].
- [78] T. Senior, Impedance boundary conditions for imperfectly conducting surfaces, *Appl. Sci. Res., Sect. B* **8**, 418 (1960).
- [79] N. Klein, H. Chaloupka, G. Müller, S. Orbach, H. Piel, B. Roas, L. Schultz, U. Klein, and M. Peiniger, The effective microwave surface impedance of high- $T_c$  thin films, *J. Appl. Phys.* **67**, 6940 (1990).
- [80] D. C. Mattis and J. Bardeen, Theory of the anomalous skin effect in normal and superconducting metals, *Phys. Rev.* **111**, 412 (1958).
- [81] K. K. Mei and G.-C. Liang, Electromagnetics of superconductors, *IEEE Trans. Microw. Theory Tech.* **39**, 1545 (1991).
- [82] D. M. Sheen, S. M. Ali, D. E. Oates, R. S. Withers, and J. Kong, Current distribution, resistance, and inductance for superconducting strip transmission lines, *IEEE Trans. Appl. Supercond.* **1**, 108 (1991).
- [83] Release 2021 R2, HFSS, Ansys, Canonsburg, Pennsylvania (2021).
- [84] S. K. Tolpygo, E. B. Golden, T. J. Weir, and V. Bolkhovskiy, Mutual and self-inductance in planarized multilayered superconductor integrated circuits: Microstrips, striplines, bends, meanders, ground plane perforations, *IEEE Trans. Appl. Supercond.* **32**, 1 (2022).
- [85] J. C. Swihart, Field solution for a thin-film superconducting strip transmission line, *J. Appl. Phys.* **32**, 461 (1961).
- [86] S. M. Anlage and D. H. Wu, Magnetic penetration depth measurements in cuprate superconductors, *J. Supercond.* **5**, 395 (1992).
- [87] O. Rocha, C. Viana, L. C. D. Gonçalves, and N. Morimoto, Electrical characteristics of PECVD silicon oxide deposited with low TEOS contents at low temperatures, *Proceedings - Electrochemical Society* **3**, 295 (2004).
- [88] H. Luo, Ph.D. thesis, The Graduate School of the University of Maryland, University of Maryland, 2021. <https://doi.org/10.13016/mrpe-2lkk>.
- [89] A. Khanna and Y. Garault, Determination of loaded, unloaded, and external quality factors of a dielectric resonator coupled to a microstrip line, *IEEE Trans. Microw. Theory Tech.* **31**, 261 (1983).
- [90] D. R. Cote, S. Nguyen, W. J. Cote, S. L. Pennington, A. K. Stamper, and D. V. Podlesnik, Low-temperature chemical vapor deposition processes and dielectrics for microelectronic circuit manufacturing at IBM, *IBM J. Res. Dev.* **39**, 437 (1995).
- [91] C. C. Chin, D. E. Oates, G. Dresselhaus, and M. S. Dresselhaus, Nonlinear electrodynamics of superconducting NbN and Nb thin films at microwave frequencies, *Phys. Rev. B* **45**, 4788 (1992).
- [92] W. Jutzi, S. Wuensch, E. Crocoll, M. Neuhaus, T. Scherer, T. Weimann, and J. Niemeyer, Microwave and dc properties of niobium coplanar waveguides with 50-nm linewidth on silicon substrates, *IEEE Trans. Appl. Supercond.* **13**, 320 (2003).
- [93] P. J. Petersan and S. M. Anlage, Measurement of resonant frequency and quality factor of microwave resonators: Comparison of methods, *J. Appl. Phys.* **84**, 3392 (1998).
- [94] J. Gao, J. Zmuidzinas, A. Vayonakis, P. Day, B. Mazin, and H. Leduc, Equivalence of the effects on the complex conductivity of superconductor due to temperature change and external pair breaking, *J. Low Temp. Phys.* **151**, 557 (2008).
- [95] A. Gurevich, Theory of rf superconductivity for resonant cavities, *Supercond. Sci. Technol.* **30**, 034004 (2017).

- [96] W. Bauer, S. Giordano, and H. Hahn, Measured frequency dependence of the surface resistance of superconducting niobium, *J. Appl. Phys.* **45**, 5023 (1974).
- [97] R. C. Dynes, V. Narayanamurti, and J. P. Garno, Direct measurement of quasiparticle-lifetime broadening in a strong-coupled superconductor, *Phys. Rev. Lett.* **41**, 1509 (1978).
- [98] A. Gurevich, Tuning microwave losses in superconducting resonators, *Supercond. Sci. Technol.* **36**, 063002 (2023).
- [99] A. Philipp and J. Halbritter, Investigation of the gap edge density of states at oxidized niobium surfaces by rf measurements, *IEEE Trans. Magn.* **19**, 999 (1983).
- [100] A. K. Jonscher, The “universal” dielectric response, *Nature* **267**, 673 (1977).
- [101] J. Baker-Jarvis, M. D. Janezic, B. Riddle, and S. Kim, in *CPEM 2010* (IEEE, 2010), p. 289.
- [102] A. R. Sass and I. D. Skurnick, Current distribution in a thin-film superconducting strip transmission line, *J. Appl. Phys.* **36**, 2260 (1965).
- [103] W. Chang, The inductance of a superconducting strip transmission line, *J. Appl. Phys.* **50**, 8129 (1979).
- [104] Y. Guo, D. Kim, J. He, S. Yong, Y. Liu, X. Ye, and J. Fan, in *2020 IEEE International Symposium on Electromagnetic Compatibility & Signal/Power Integrity (EMCSI)* (IEEE, 2020), p. 422.
- [105] The recent HFSS version permitting material with complex conductivity, which removes the need for PEC ports, was unavailable at the time of this work.
- [106] T. M. Mishonov, Predicted plasma oscillations in the  $\text{Bi}_2\text{Sr}_2\text{CaCu}_2\text{O}_8$  high-temperature superconductor, *Phys. Rev. B* **44**, 12033 (1991).
- [107] For conventional superconductors such as niobium,  $\omega_p \sim 10^{15}$  Hz lies well above the superconductor gap frequency.
- [108] R. Glover III and M. Tinkham, Conductivity of superconducting films for photon energies between 0.3 and  $40 kT_c$ , *Phys. Rev.* **108**, 243 (1957).
- [109] Here, replacing  $-i\sigma_2$  with  $\sigma_1 - i\sigma_2$  recovers a superconductor complex relative permittivity,  $\epsilon_{sc} = -i\sigma/\epsilon_0\omega$ , corresponding to the intrinsic impedance  $Z_s \equiv \sqrt{\mu_0\mu_{sc}/\epsilon_0\epsilon_{sc}} = \sqrt{i\mu_0\omega/\sigma}$ , where  $\mu_{sc} = 1$  is the superconductor permeability.
- [110] C. A. T. Garcia, Ph.D. thesis, The Graduate School of the University of Maryland, University of Maryland, 2022. <https://doi.org/10.13016/lzeu-4ecp>.
- [111] S. Ramo, J. R. Whinnery, and T. Van Duzer, *Fields and Waves in Communication Electronics* (John Wiley & Sons, Hoboken, NJ, USA, 1994).
- [112] L. R. Group, *SRIMP*, Cornell University, <https://www.classe.cornell.edu/~liepe/webpage/researchsrimp.html> (2012).
- [113] M. Delheusy, A. Stierle, N. Kasper, R. P. Kurta, A. Vlad, H. Dosch, C. Antoine, A. Resta, E. Lundgren, and J. Andersen, X-ray investigation of subsurface interstitial oxygen at Nb/oxide interfaces, *Appl. Phys. Lett.* **92**, 101911 (2008).
- [114] J. K. Hulm, C. K. Jones, R. A. Hein, and J. W. Gibson, Superconductivity in the TiO and NbO systems, *J. Low Temp. Phys.* **7**, 291 (1972).
- [115] A. Gurevich and T. Kubo, Surface impedance and optimum surface resistance of a superconductor with an imperfect surface, *Phys. Rev. B* **96**, 184515 (2017).
- [116] For the N-layer subject to local electrodynamics, the impedance transformation method [52] of Appendix D yields  $R_{bl} = \omega^2\mu_0^2\lambda_h(\lambda_h + t)t\sigma_n + R_h$ , assuming  $t \ll \delta_{sk}$ , assuming  $\delta_{sk}$  is the metal skin depth.
- [117] L. N. Cooper, Superconductivity in the neighborhood of metallic contacts, *Phys. Rev. Lett.* **6**, 689 (1961).
- [118] M. S. Pambianchi, S. N. Mao, and S. M. Anlage, Microwave surface impedance of proximity-coupled Nb/Al bilayer films, *Phys. Rev. B* **52**, 4477 (1995).
- [119] A. Gurevich, private communication.
- [120] T. Oseroff, Z. Sun, and M. U. Liepe, Measurements of the amplitude-dependent microwave surface resistance of an Au/Nb bilayer, *Supercond. Sci. Technol.* **36**, 115009 (2023).
- [121] S.-P. Ju, C.-I. Weng, J.-G. Chang, and C.-C. Hwang, Molecular dynamics simulation of sputter trench-filling morphology in damascene process, *J. Vac. Sci. Technol., B: Microelectron. Nanometer Struct.—Process., Meas., Phenom.* **20**, 946 (2002).
- [122] A. Romanenko, C. Edwardson, P. Coleman, and P. Simpson, The effect of vacancies on the microwave surface resistance of niobium revealed by positron annihilation spectroscopy, *Appl. Phys. Lett.* **102**, 232601 (2013).
- [123] J. Lee, Z. Sung, A. A. Murthy, M. Reagor, A. Grassellino, and A. Romanenko, Discovery of Nb hydride precipitates in superconducting qubits, [arXiv:2108.10385](https://arxiv.org/abs/2108.10385) (2021).
- [124] EAG Laboratories, [www.eag.com](http://www.eag.com) (2022).
- [125] A. Sass and W. Stewart, Self and mutual inductances of superconducting structures, *J. Appl. Phys.* **39**, 1956 (1968).
- [126] L. A. Vainshtein, *Electromagnetic Waves* (Moscow, Izdatel'stvo Radio i Sviaz', in Russian, 1988), 2nd ed.
- [127] A. V. Varganov, E. A. Vopilkin, P. P. Vysheslavtsev, Y. N. Drozdov, Y. N. Nozdrin, S. A. Pavlov, A. E. Parafin, and V. V. Talanov, Structure and transport properties of ultrathin  $\text{YBa}_2\text{Cu}_3\text{O}_{7-x}$  films, *J. Exp. Theor. Phys. Lett.* **63**, 644 (1996). [In Russian—*Pis'ma Zh. Eksp. Teor. Fiz.* **63**, 608 (1996)].
- [128] T. Van Duzer and C. W. Turner, *Principles of Superconductive Devices and Circuits* (Prentice Hall, Philadelphia, Pennsylvania, 1998), 2nd ed.
- [129] J. Zmuidzinas, Superconducting microresonators: Physics and applications, *Annu. Rev. Condens. Matter Phys.* **3**, 169 (2012).
- [130] V. V. Talanov, Electrodynamics of the Josephson-coupled parallel plate resonator, [arXiv:1108.2697](https://arxiv.org/abs/1108.2697) (2011).
- [131] C. R. Paul, *Analysis of Multiconductor Transmission Lines* (John Wiley & Sons, Hoboken, NJ, USA, 2007).